

Modeling waves and wind stress

M. A. Donelan,¹ M. Curcic,¹ S. S. Chen,¹ and A. K. Magnusson²

Received 28 November 2011; revised 17 May 2012; accepted 21 May 2012; published 17 July 2012.

[1] A model for wave and wind stress prediction is constructed. The source functions that drive the space-time evolution of the energy spectra are developed in form based on theory and laboratory and field experiments. The calibration factors (proportionality constants of the source functions) are determined from a comparison of modeled and observed significant height and mean period. The observations are for the month of January 2005 and are derived from an array of laser range finders mounted on a bridge between two platforms in the Ekofisk oil field in the North Sea. The model calculates the form stress on the waves and adds it vectorially to the sheltering-modified skin stress. The resulting drag coefficient versus wind speed is shown to have the observed structure: low in light winds, increasing in moderate winds, and increasing more slowly in very strong winds. Modeled spectral shapes in the four quadrants of Hurricane Bonnie (1998) match the Scanning Radar Altimeter measurements. Modeled spectral properties in Hurricane Ike (2008) are compared against NDBC buoy estimates with good results. Drag coefficients in the mixed seas produced by hurricanes show dependence on wave age of the wind sea, swell propagation direction, and water depth. The need for wave and stress modeling for atmosphere-ocean coupling is emphasized. The new wave model has all the necessary attributes to be the basis for such a coupler.

Citation: Donelan, M. A., M. Curcic, S. S. Chen, and A. K. Magnusson (2012), Modeling waves and wind stress, *J. Geophys. Res.*, 117, C00J23, doi:10.1029/2011JC007787.

1. Introduction

[2] The drag or momentum transfer between atmosphere and oceans is of two types, namely: the frictional or “skin” drag and the wave or “form” drag. The skin drag comes about through the direct molecular interaction at the interface. The form drag arises from the form of the waves and becomes larger as the steepness (or mean square slope) of the waves increases. The steeper the waves the larger the contribution of the wave drag to the total drag. In a fully developed sea the large waves at the spectral peak propagate close to the wind speed and therefore do not contribute much form drag; in this situation the roughness elements are the steep shorter waves in the equilibrium range above the spectral peak. At winds in excess of 5 m/s the equilibrium waves are quasi-saturated, meaning that their steepness, being limited by breaking, does not increase much with increasing wind speed. Nonetheless the fully developed form drag increases with wind speed because more longer waves are in the equilibrium range and contribute to the form drag.

In storm conditions or at short fetch or in shoaling conditions the spectral peak waves can be very steep and may contribute a significant fraction of the form drag. This contribution is not simply related to the wind speed but rather depends on the state of development of the waves.

[3] The task of coupling atmosphere and oceans, especially in storms, requires rather detailed knowledge of the wavefield and, in particular, the momentum transfer between boundary layer winds and surface waves. As pointed out by Mellor *et al.* [2008], state-of-the-art wave models require about two orders of magnitude more computational effort than oceanic circulation models. This makes them unsuitable for direct atmosphere-wave-ocean coupling. In this paper we address the modeling of waves and wind stress in the general case. We are motivated to address this topic by the perceived need for a faster wave model to provide full atmosphere-wave-ocean coupling in attempting to forecast the development and track of hurricanes. The extreme conditions in hurricanes require coupling information at small spatial scales (<5 km) and small time intervals (<5 min) over a large domain in which the storm propagates.

¹Rosenstiel School of Marine and Atmospheric Science, University of Miami, Miami, Florida, USA.

²Norwegian Meteorological Institute, Bergen, Norway.

Corresponding author: M. A. Donelan, Rosenstiel School of Marine and Atmospheric Science, University of Miami, 4600 Rickenbacker Causeway, Miami, FL 33149, USA. (mdonelan@rsmas.miami.edu)

©2012. American Geophysical Union. All Rights Reserved.
0148-0227/12/2011JC007787

2. The Wave Model

2.1. The Energy Balance Equation

[4] The wave model is formulated in terms of the spectrum of elevation variance by wave number, k , and propagation direction, ϕ , $E(k, \phi)$. [The energy spectrum is just the variance spectrum times liquid density, ρ_w and the acceleration due

to gravity, g]. The energy balance equation in a basin of varying depth is:

$$\frac{\partial E'}{\partial t} + \frac{\partial[E'(c_g \cos \phi + u)]}{\partial x} + \frac{\partial[E'(c_g \sin \phi + v)]}{\partial y} + \frac{\partial(\dot{k}E')}{\partial k} + \frac{\partial(\dot{\phi}E')}{\partial \phi} = \rho_w g \sum_{i=1}^n S_i \quad (1)$$

where $E'(k, \phi)$ is the energy spectrum and $E(k, \phi)$ is the variance spectrum, c_g is the group speed in the direction ϕ and u, v are the components of the average current in the wave boundary layer at depth $= 0.5/k$ [Fan et al., 2009]; the fourth term on the left-hand side is advection in wave number space, and is negligible for slowly varying current fields or bottom topography; the fifth term on the left-hand side is advection in directional space (refraction), and is nonzero for a sloped bottom or a spatially inhomogeneous current field; $\sum_{i=1}^n S_i$ are the source/sink functions that act to grow/decay the waves locally.

[5] The energy spectrum and the variance spectrum are related by:

$$E'(k, \phi) = \rho_w g E(k, \phi) \quad (2)$$

So that the variance of surface elevation, σ^2 is:

$$\sigma^2 = \iint E(k, \phi) k dk d\phi \quad (3)$$

2.2. Physical Processes

[6] There are eleven identifiable physical processes that have a first-order effect on the wave energy spectrum of wind-generated waves:

[7] 1. Wind input: The wind may add to or subtract from the momentum of existing waves.

[8] 2. Wave breaking: The breaking of waves of all wavelengths produces a net loss of energy from the wave-field to turbulence and a conversion of wave momentum to current momentum.

[9] 3. Resonant wave-wave interactions: Energy is moved from one part of the spectrum to another. This process may be conservative, having no net loss or gain of energy over the spectrum, as it is in the theoretical weak interaction of a resonant quartet of gravity waves.

[10] 4. Strong nonlinear interactions: Wave breaking is a strongly nonlinear interaction in which wave energy is passed from the breaking wave to turbulence and to adjacent shorter and longer waves [Pierson et al., 1992]. The net effect, of this broadening of the spectrum in a saturated spectrum, is a shift of energy to longer waves than the peak. Thus, this is a source function to waves on the forward face of the spectrum.

[11] 5. Nonlinear wave evolution: The frequency down-shift of wave energy also occurs in nonlinear (but not breaking) waves [Huang et al., 1996; Trulsen and Dysthe,

1997; Dysthe et al., 2003] and is distinct from the down-shifts associated with resonant wave-wave interactions or wave breaking.

[12] 6. Dissipation by turbulence: Turbulence in the wave boundary layer dissipates wave energy preferentially for shorter waves.

[13] 7. Dissipation by viscosity: Liquid viscosity in the surface viscous sublayer acts to dissipate waves preferentially as k^2 .

[14] 8. Wave breaking in shallow water: Waves break when they become too steep and the steepness is enhanced by shoaling and the breaking intensity is related to non-linearity and to kd , the depth (d) to wavelength (λ) ratio: $kd = 2\pi d/\lambda$.

[15] 9. Bottom interaction: The orbital velocities of long waves interact with the bottom. Generally there is a loss of energy from the long waves.

[16] 10. Long wave to short wave interaction: Long waves passing through a field of short waves cause convergences and divergences, enhancing and suppressing wave breaking of the short waves. Quasi-saturated waves in the equilibrium range suffer a net reduction in energy caused by the waves at the spectral peak and longer [Donelan et al., 2010].

[17] 11. Wave-current interaction: The interaction of waves with the average (over the wave boundary layer) current is described by the second and third terms in equation (1).

[18] Source functions corresponding to these eleven processes are devised (section 2.3) and calibrated against field data in the North Sea (section 3.1).

[19] The model includes shoaling and refraction induced by changes in bottom topography or ambient currents, and dissipation of energy on beaches. It does not include diffraction around breakwaters, reflection from boundaries and triad interactions in the surf zone.

2.3. Functional Form of the Source Functions

[20] The source functions S_i are parametric descriptions of the various phenomena that increase, decrease or interchange among wave numbers the energy in the wave number spectrum. The wave number spectrum is evaluated in separable magnitude and direction bins. We seek the fewest and simplest source functions that mimic the observed phenomena that occur in the evolution of wind-generated waves. There are two compelling reasons for this parsimony: Occam's razor argues for minimizing the number of hypotheses necessary to reproduce observable behavior; and the goal of computational efficiency is particularly important in models that forecast conditions that may be dangerous to life or property. We rely on theory and laboratory and field experiments to provide the form of the source functions and comparisons with field data to quantify them.

[21] The first term of the energy balance equation (1) expresses the time evolution of the local spectrum and is of the form: $\rho_w g \omega E(k, \phi)$. The second and third terms express the spatial evolution of the spectrum times the vector sum of the group velocity and the current and are of the form: $\rho_w g k(c_g + u)E(k, \phi)$. Note also that $c_g = \text{function}(kd)$.

[22] It follows, therefore, that the S_i must have either form and may, in addition, depend on functions of nondimensional

ratios of the various relevant variables. The variables of interest are as follows:

- $U_{\lambda/2}$ the wind speed at a height of one half wavelength, $\lambda/2$;
- k wave number of a wave, $k = 2\pi/\lambda$,
- ω frequency of a wave of wave number, k ; $\omega = kc$,
- c phase speed of a wave of wave number, k ,
- c_g group speed of a wave of wave number, k ,
- E wave number–directional variance spectrum,
- d local depth of fluid,
- g acceleration due to gravity,
- ρ_a gas density,
- ρ_w liquid density.

[23] The nondimensional ratios of interest are as follows:

- $\frac{\rho_a}{\rho_w}$ fluid density ratio, reflects strength of forcing for a given wind,
- $\frac{U_{\lambda/2}}{c}$ wind forcing of waves in wind direction,
- $\frac{U_{\lambda/2} \cos \theta}{c} - 1$ wind forcing, considering angle between waves and wind, θ (forcing vanishes when wind component in wave propagation direction equals phase speed),
- $k^4 E$ saturation spectrum, reflects tendency to break,
- kd depth/wavelength ratio, reflects bottom effects.

2.3.1. S_{in} : The Wind Input Source Function

[24] *Jeffreys's* [1924, 1925] sheltering hypothesis leads to S_{in} of the form:

$$S_{in} = A_1 (U_{\lambda/2} \cos \theta - c - u \cos \phi - v \sin \phi) |U_{\lambda/2} \cos \theta - c - u \cos \phi - v \sin \phi| \frac{k\omega}{g} \frac{\rho_a}{\rho_w} E(k, \phi) \quad (4)$$

where θ is the angle between wind direction, ψ , and waves of wave number, k and direction, ϕ . A_1 is the sheltering coefficient.

[25] S_{in} is positive (energy and momentum transferred from wind to waves) when $U_{\lambda/2} \cos \theta > c + u \cos \phi + v \sin \phi$, and negative (energy and momentum transferred from waves (swell) to wind) when $0 < U_{\lambda/2} \cos \theta < c + u \cos \phi + v \sin \phi$ or when the waves (swell) propagate against the wind, $\cos \theta < 0$. As waves approach full development S_{in} goes to zero; that is, the direct wind forcing vanishes. The sheltering coefficient, which describes the strength of the source/sink function, is different depending on whether S_{in} is positive (wind sea) or negative, when the waves run before the wind or against it (swell). The wind velocity is that at one half wavelength above the surface up to the top of the logarithmic layer, which is usually taken to be 20 m in the field.

[26] *Jeffreys's* sheltering hypothesis has been verified in both laboratory and field measurements of the direct momentum transfer between wind and waves [*Hsiao and Shemdin*, 1983; *Donelan*, 1999; *Donelan et al.*, 2006]. The sheltering coefficient, A_1 ranges from 0.12 to 0.28 with no clear dependence on scale. Here we take A_1 to be an adjustable parameter initially. It is set by running the model with basin-scale winds and wave verification data (see section 3). The choice of A_1 affects both the predicted wave spectrum and the calculated wind stress.

2.3.2. Wind Stress

[27] Energy and momentum in the wavefield are related by the phase speed: $E' = Mc$, so that the form drag components (x , y or east and north) of the wind on the waves are calculated from the wind input source function integrated over the spectrum:

$$\tau_x = \rho_w g \int_{-\pi}^{\pi} \int_{k_{\min}}^{k_{\max}} \frac{S_{in}}{c} \cos \phi k dk d\phi \quad (5)$$

$$\tau_y = \rho_w g \int_{-\pi}^{\pi} \int_{k_{\min}}^{k_{\max}} \frac{S_{in}}{c} \sin \phi k dk d\phi \quad (6)$$

[28] To capture the full form stress the integrals (5) and (6) should be evaluated up to $k_{\max} = 1000 \text{ m}^{-1}$ (6.3 mm wavelength), where the spectrum falloff is rapid [*Donelan et al.*, 2010]. For computational efficiency the model is run with $f_{\max} = 2 \text{ Hz}$ and a tail of slope ts is appended to the spectral value at the highest wave number (k_{\max} corresponding to f_{\max}) and the integral evaluated over the tail out to $k_{\text{cutoff}} = 1000$. The slope of the tail [$S(k) = S(k_{\max})(k/k_{\max})^{ts}$] was determined by running the model at various wind speeds (U_{10}) from 5 to 55 m/s with $f_{\max} = 2 \text{ Hz}$:

$$ts = -1.0186 - 0.01451U_{10} + 0.000112U_{10}^2 \quad (7)$$

where U_{10} is in m/s.

[29] If $f_{\max} < 2 \text{ Hz}$, say 0.5 Hz, the contribution to the form stress from the tail will be slightly underestimated. This will not significantly affect the wave predictions but, of course, the coupling with the atmosphere will be weakened. Therefore, coupled runs should have $f_{\max} = 2 \text{ Hz}$.

[30] The form drag coefficient, Cd_f is then calculated:

$$Cd_f = \frac{\sqrt{\tau_x^2 + \tau_y^2}}{\rho_a U_z^2} \quad (8)$$

where U_z is the wind at the measured or modeled height.

[31] Clearly the calculated form drag coefficient is directly proportional to the sheltering coefficient, A_1 . Thus, consistency with measured drag coefficients provides close constraints on the acceptable value of A_1 .

[32] The skin drag coefficient, Cd_s , in the absence of waves, is then calculated from the law of the smooth wall using the vector difference of wind velocity and surface current. The skin drag is in the direction of the wind minus current vector. The form drag is in the wave direction, ϕ or against it in the case of swell propagating upwind.

[33] In the presence of waves the skin drag coefficient is reduced due to the sheltering of the surface in the lee of steep waves. The degree of sheltering of the skin is taken to be proportional to the ratio of total drag to skin drag and may be as large as 50% corresponding to full sheltering of the lee face of each wave. The algorithm for the adjusted skin drag coefficient, Cd'_s is as follows:

$$Cd'_s = \frac{Cd_s}{3} \left(1 + \frac{2Cd_s}{Cd_s + Cd_f} \right) \quad (9)$$

The total stress components are calculated by adding the previously calculated form stress components to the adjusted skin stress components:

$$\tau'_x = \tau_x + \rho_a C d'_s U_z^2 \cos \psi \quad (10)$$

$$\tau'_y = \tau_y + \rho_a C d'_s U_z^2 \sin \psi \quad (11)$$

These are the stress components of the wind on the surface. They are the mechanical couplers with the atmospheric model.

[34] At low wind speeds the stress is largely skin stress. As the wind speed increases and the waves grow the form stress exceeds the skin stress until in very strong winds the form stress accounts for most of the tangential stress on the surface and may differ in direction from the wind vector toward the propagation direction of the peak of the wind sea. Shoaling of the peak of the wind sea reduces the phase velocity and increases the amplitude thereby increasing the form stress yielding a bigger elevation surge than would be obtained assuming a strictly wind speed-dependent stress.

$$A_1 = \begin{cases} 0.11, & \text{if } U_{\lambda/2} \cos \theta > c + u \cos \phi + v \sin \phi, \text{ wind sea} \\ 0.01, & \text{if } 0 < U_{\lambda/2} \cos \theta < c + u \cos \phi + v \sin \phi, \text{ swell with wind} \\ 0.1, & \text{if } \cos \theta < 0, \text{ swell against wind} \end{cases} \quad (12)$$

[35] The numerical values of A_1 are established in sections 3 and 4 by comparison of modeled and observed wave spectra.

2.3.3. S_{dv} : Dissipation by Viscosity

[36] Some wave energy is converted directly to heat through the action of the viscosity of the liquid. Viscous dissipation in the surface sublayer prevents the growth of waves until a threshold wind speed is exceeded. The theoretical viscous dissipation rate, $4\nu k^2$, has been verified in the laboratory for a range of viscosities, ν [Donelan and Plant, 2009].

$$S_{dv} = -4\nu k^2 E(k, \phi) \quad (13)$$

[37] It is negligible in clean water for all but the shortest waves ($\lambda < 20$ cm).

2.3.4. S_{ds} : The Wave Dissipation Source Function

[38] It is generally accepted that most of the dissipation of wave energy through conversion to turbulence is brought about by wave breaking. Once the wind exceeds the threshold for a particular wavelength, input exceeds dissipation and the waves grow until limited by breaking. Initially no air is entrained and so the breaking of these capillary gravity waves, while dissipative, produces no whitecaps. Spilling breakers occur at the crest of a wave and persist for a fraction of the wave's period, releasing about one third of the wave's energy. They are sporadic and their density (number per unit area) increases as the energy (from the wind) to be dissipated increases. Waves break in a narrow range of steepness (height over wavelength) of $0.1 < \frac{H}{\lambda} < 0.15$. This is the usual pattern in deep water. When waves shoal they undergo rapid energy flux convergence for which "spilling" breaking may

not be dissipative enough to limit the steepness. In this circumstance they break in "plunging," losing energy much more rapidly and, if the shoaling energy convergence persists, so does the plunging as the wave sweeps through the surf zone.

[39] Plunging is far more dissipative than spilling but both forms of breaking act to limit the steepness. This limiting effect of breaking leads to the existence of an equilibrium or quasi-saturation range in wind-wave spectra for wavelengths shorter than the spectral peak [Phillips, 1977]. The expected and observed spectral shape in this range is proportional to k^{-4} [Phillips, 1977], so that the degree of saturation, $B(k, \phi)$ is given by:

$$B(k, \phi) = k^4 E(k, \phi) \quad (14)$$

The dissipation sink function may therefore be written [Donelan, 2001]:

$$S_{ds} = -A_2 [B(k, \phi)]^n \omega(k) E(k, \phi) \quad (15)$$

We further note that the longer waves modulate the shorter waves increasing the dissipation at convergences of the long

waves' orbital velocities, while reducing the dissipation at orbital velocity divergences [Phillips, 1977; Donelan, 2001; Donelan et al., 2010]. If n in (15) is larger than 0, the net effect is to increase the dissipation by an amount proportional to the mean square slope of the longer waves. By balancing input against dissipation, Donelan [2001] obtained a dissipation function for spilling breakers, S_{sb} , of the form:

$$S_{sb} = -A_2 [1 + A_3 \chi^2(k, \phi)]^2 [B(k, \phi)]^{2.5} \omega(k) E(k, \phi) \quad (16)$$

where χ^2 is the mean square slope in the direction, ϕ , of all waves longer than $\lambda(k)$.

[40] To account for the increased dissipation due to plunging breakers in the shoaling areas we increase the multiplier, A_2 by the horizontal-to-vertical orbital velocity enhancement in shallow water, $\coth kd$. The complete wave breaking dissipation sink function is:

$$S_{ds} = \coth kd S_{sb} = -A_2 \coth kd [1 + A_3 \chi^2(k, \phi)]^2 \cdot [B(k, \phi)]^{2.5} \omega(k) E(k, \phi) \quad (17)$$

[41] This dissipation sink function incorporates three physical processes:

[42] 1. The tendency of the spectra to quasi-saturation, i.e., k^{-4} spectral falloff in the equilibrium range. The nonlinear dependence of S_{ds} on the degree of saturation tends to cause equilibration to k^{-4} spectral falloff, as observed [Donelan et al., 2010].

[43] 2. The mean square slope of the waves at the spectral peak reduces the spectral densities in the equilibrium range relative to the peak, the well-known “overshoot” phenomenon. In strongly forced conditions the waves at the spectral peak are steeper than those in the equilibrium range [Hasselmann *et al.*, 1973; Donelan *et al.*, 1985, 2010].

[44] 3. Shoaling waves dissipate more rapidly than deep water spilling breakers. The dissipation rate increases as the horizontal-to-vertical orbital velocity enhancement, $\coth kd$. This has the effect of limiting the ratio of breaker height to depth in shoaling waves.

2.3.5. S_{dt} : Dissipation by Turbulence

[45] Turbulence mixing in the wave boundary layer attenuates waves. By analogy with the viscous dissipation we set:

$$S_{dt} = -4\nu_t k^2 E(k, \phi) \quad (18)$$

where ν_t is the turbulent kinematic viscosity or eddy viscosity.

[46] ν_t is proportional to friction velocity in the water, u_{*w} , and is an average over depth proportional to the wavelength, λ :

$$\nu_t \propto u_{*w}/k \quad (19)$$

So that the sink function for dissipation by turbulence is modeled as:

$$S_{dt} = -A_4 u_{*w} k E(k, \phi) \quad (20)$$

2.3.6. S_{nl} : The Nonlinear Interaction Source Function

[47] Even in light winds the waves in the equilibrium range are quasi-saturated and limited by breaking. The waves that break have exceeded some critical steepness and are nonlinear. In general gravity waves propagate in groups and break with a periodicity of about twice as long as the period of the central frequency of the group [Donelan *et al.*, 1972]. This low-frequency train of impulses (“whitecaps”) signals frequency downshifting. Pierson *et al.* [1992] measured the spectral changes associated with the breaking of coalescing groups in a tank. They found that, while wave energy is dissipated, a comparable amount is passed to lower and higher frequencies; that is, the spectrum is both reduced and broadened. In a quasi-saturated spectrum, energy passed to higher frequencies is dissipated by enhanced wave breaking of these shorter waves, while energy passed to lower frequencies adds to the growth of these longer unsaturated waves. The former transfer may be subsumed into the dissipation source function, while the latter requires a flow of energy to lower frequencies, an additional growth term that acts to promote the growth of waves below the frequency of the spectral peak. These waves are amplified by the wind, resulting in a downshift of the spectral peak.

[48] It is clear that wave breaking by spilling and downshifting are related phenomena and we therefore construct a nonlinear interaction source function that passes energy to longer waves. While the quantitative relation between downshifting and spilling breaking has not yet been established, it appears that the energy passed to lower frequencies

increases with the wave breaking intensity and decreases with the separation frequency. In the model, two immediately lower wave numbers receive energy in such a way that energy is distributed nearly evenly if the relative separation frequency is small, and preferentially to the closer frequency if the relative separation frequency is large. The algorithm in the model follows these guidelines: a quantity of energy, proportional to the energy dissipated, is passed to longer waves in the next two lower wave number bins. The amount transferred decays exponentially with the square of the relative frequency separation. The modeled process is conservative with a net transfer of energy across the spectral peak from higher wave numbers to lower wave numbers:

$$S_{nl}(k, \phi) = A_5 [b_1 S_{sb}(k - \Delta k, \phi) + b_2 S_{sb}(k - 2\Delta k, \phi) - S_{sb}(k, \phi)] \quad (21)$$

where $A_5 = 5$, $b_1 = \exp(-16(\frac{\Delta f}{f})^2)$, $b_2 = \exp(-16(2\frac{\Delta f}{f})^2)$, and b_1 and b_2 are normalized such that $b_1 + b_2 = 1$.

[49] Two other nonlinear interaction processes (resonant wave-wave interactions [Hasselmann, 1962, 1963a, 1963b] and nonlinear wave train evolution [Huang *et al.*, 1996; Trulsen and Dysthe, 1997; Dysthe *et al.*, 2003]) are known to occur and to produce a net shift of energy toward longer waves. Furthermore, they both are also strongly dependent on degree of nonlinearity and therefore may be represented by the algorithm devised above for the strong nonlinear interactions. A_5 , determined by comparison of model output with observations, will reflect the sum of these three nonlinear interaction processes. From a practical point of view, there is no need to model them separately and there is a high price in computational effort to be paid to attempt to calculate them theoretically.

2.3.7. S_{bf} : The Bottom Friction Source Function

[50] The bottom friction source function is related to orbital velocity at the bottom and the roughness of the bed. Komen *et al.* [1994] give the following form for a sandy bed:

$$S_{bf} = -G_f \frac{k}{\sinh 2kd} E(k, \phi) \quad (22)$$

where the roughness factor, G_f varies from 0.001 to 0.01 m/s, depending on bed roughness.

2.3.8. S_{bp} : The Bottom Percolation Source Function

[51] On a porous bed the percolation of flow through the bed induces wave energy dissipation. The dissipation rate due to percolation is given by Shemdin *et al.* [1978]:

$$S_{bp} = -G_p \frac{k}{\cosh^2 kd} E(k, \phi) \quad (23)$$

where the permeability factor, G_p varies from 0.0006 to 0.01 m/s, depending on sand grain size.

3. Quantifying the Source Functions

[52] At this stage the forms of the source functions have been established by a combination of theoretical ideas and dimensional analysis. It remains to determine five proportional constants: A_1 , A_2 , A_3 , A_4 and A_5 . We will do this by comparison of the model output (given well analyzed winds)

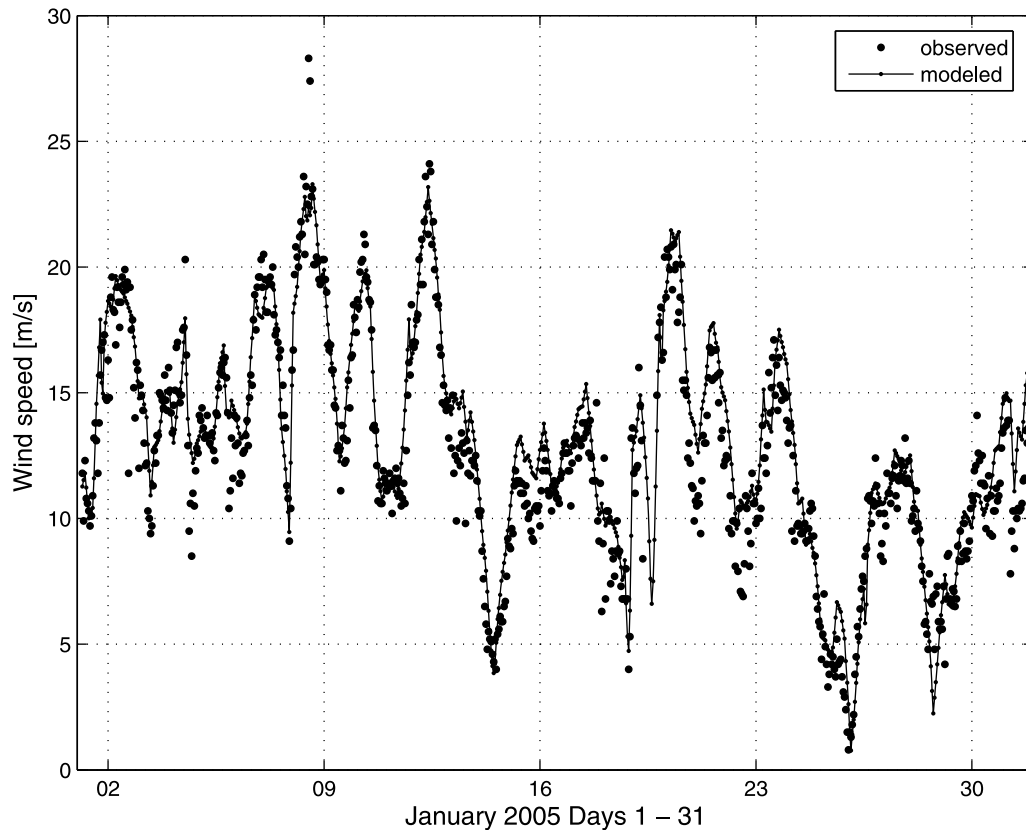


Figure 1. Time series of observed and modeled wind speed at Ekofisk, January 2005.

with observations. Henceforth the University of Miami Wave Model is referred to by its acronym: “UMWM.”

3.1. North Sea Tests

[53] The North Sea is one of the stormiest bodies of water on the planet. Frequent Atlantic depressions moving east produce wind speeds in excess of 15 m/s and significant wave heights in excess of 4 m. Norway has several oil and gas production platform complexes in the adjoining North and Norwegian Seas, and the Norwegian Meteorological Institute (<http://www.met.no>) invests much time and effort in providing operational forecasts and well-analyzed meteorological hindcasts for the safety and design of structures in its territorial waters. The month of January 2005 was particularly stormy and was selected to compare hindcasted model output with wave observations to determine the proportionality constants. The wave observations were made in the Ekofisk field in the North Sea. The UMWM model was run with analyzed wind fields from the NORA10 hindcast database [Reistad *et al.*, 2007, 2011] provided by the Norwegian Meteorological Institute. The hindcast area extends over the northeastern Atlantic, the Nordic Seas and the Barents Sea with a horizontal resolution of 10 km. Wind fields are from the atmospheric model HIRLAM [Unden *et al.*, 2002], interpolated to 0.1° and extending from 15W, 51.5N to 25E, 75N. The analyzed winds are on a 3-hourly interval and are interpolated to the time step of the model. Model output, including interpolated winds, is provided at the top of each hour. The wind observations are

10 min averages every hour. A measure of the quality of the hindcasted (analyzed) winds is given by the comparison of modeled wind speeds with observations at Ekofisk (Figure 1).

[54] The wave measuring system at the Ekofisk field at 56.5°N , 3.2°E (water depth of 70 m) includes an array of four infrared laser range finders (LASAR) arranged in a square of side 2.6 m. One of the laser range finders (called laser elevation gauges or LEGs) is noticeably noisier than the others. It was left out and the triplet of good LEGs is used to determine directional spectra every 20 min throughout the month using the Wavelet Directional Method (WDM) [Donelan *et al.*, 1996]. The source function proportionality constants were adjusted to yield close agreement between model and measurements of significant height and second moment mean period, T_{M02} . T_{M02} is defined as the square root of the ratio of the zeroth moment of the frequency spectrum to the second moment. The moments are calculated between 0.03 Hz and 0.5 Hz. Significant height is affected principally by S_{in} and S_{ds} , while T_{M02} is most sensitive to S_{nl} . The source function proportionality constants are as follows: S_{in} from wind to waves, $A_1 = 0.11$; S_{ds} overall, $A_2 = 42$; S_{ds} mean square slope, $A_3 = 120$; S_{dt} , $A_4 = 0.01$; and S_{nl} , $A_5 = 5$.

[55] The wind input term is strong for wind sea, waves propagating downwind and slower than the wind. Waves propagating against or faster than the wind (swell) are less strongly coupled with the wind. The values of A_1 in these two swell cases are determined in the hurricane tests (section 4), where swell and counterc swell are quite common.

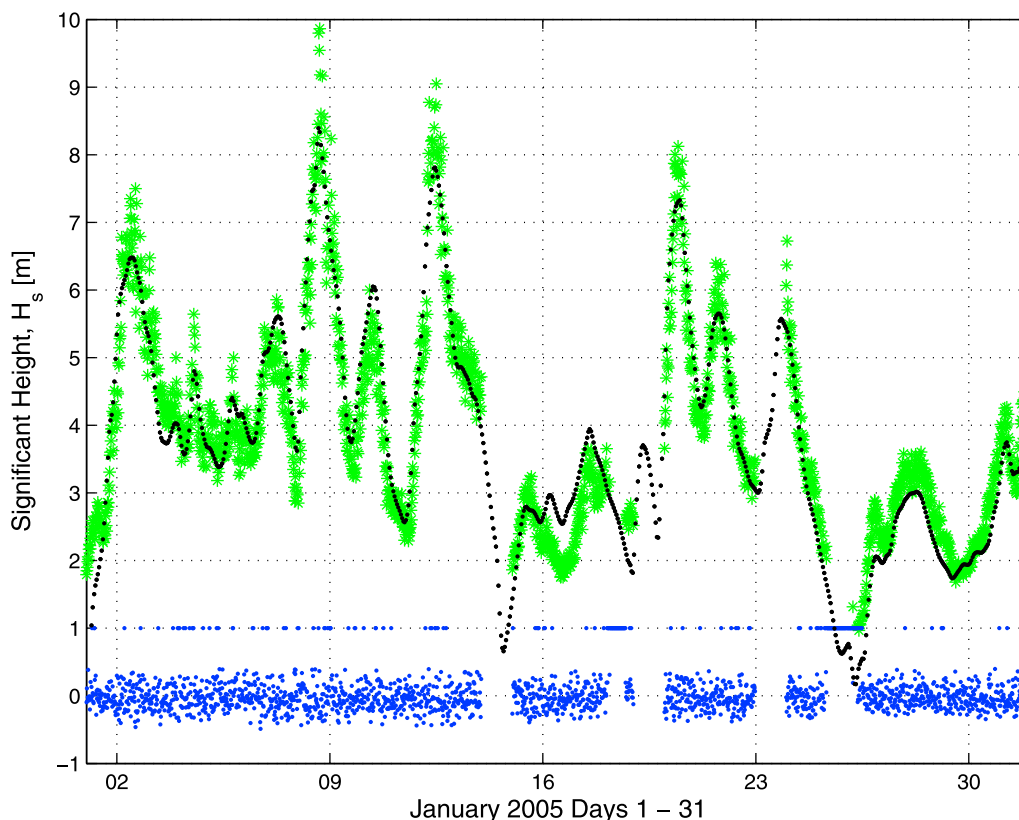


Figure 2. Time series of observed (green asterisks) and modeled (black dots) significant heights, H_s , at Ekofisk, January 2005. The observations were made with LASAR, an array of laser range finders on the corners of a square of side 2.6 m. The blue dots are the kurtosis -3 of the surface elevation observations; values greater than 0.4 are not used in the regression analysis in Figure 3.

[56] The dissipation term is highly nonlinear and acts to keep waves from becoming too steep, i.e., maintains the strongly forced waves in a quasi-saturated state.

[57] The nonlinear transfer of energy to lower frequencies is proportional to the spilling dissipation term, and the amount of energy transferred is five times that dissipated. This strong flux of energy to lower frequencies (or “down-shifting”) is the principal agent of the development of wave period.

[58] A comparison of the measured and predicted significant wave heights is given in Figure 2 as a time series, and in Figure 3 as a scatterplot of the hourly time coincident data. The measurements were made at 5 Hz per LEG and each data point is a 20 min average. The model estimates are every hour and are based on 3-hourly winds interpolated to each time step. The model takes about 12 h to spin-up (see Figures 2, 4, and 6) so that data from the first day are not included in the regressions.

[59] The laser range finders are subject to dropout errors in light winds and fog. These are easily detected and replaced if they are isolated errors. Dropout clusters are difficult to treat and they are manifest in the high kurtosis of the treated elevation signal. For typical wind seas the kurtosis is about 3. A purely Gaussian signal has a kurtosis of 3, whereas a nearly sinusoidal swell approaches 1.5 from above. Kurtosis values less than 3.4 are taken to indicate good data and these are compared with the model estimates at the same time

(kurtosis -3 values greater than 0.4 are set to 1 in the plot). Figure 2 is a time series of the modeled (black dots) and observed (green asterisks) significant heights for the month of January 2005. There are 3 days of missing data and another 2 days of consistently high kurtosis.

[60] Significant wave height is an integral parameter derived in the model by integrating the modeled spectrum over the frequency range modeled: 0.03 Hz to 0.5 Hz. In addition the contribution from an f^{-5} tail was added. In the observations significant height is just four times the standard deviation of surface elevation.

[61] The observed and modeled significant heights are shown in Figure 3 as a scatterplot. The 45° line (dashed) indicates agreement of modeled and observed. The least squares regression line (solid) has a slope of 0.96 (43.8°). At 2 m the modeled significant height is 9 cm high and at 10 m it is 23 cm low. The high points (>8 m) are underestimated by the model, perhaps because the winds are 3-hourly and likely miss the high points of the storms.

[62] The mean period, based on the second and zeroth moments of the frequency spectrum: $T_{M02} = \sqrt{\frac{m_0}{m_2}}$, is shown in Figure 4. The scatterplot of the modeled T_{M02} against the measured T_{M02} is Figure 5. The least squares regression line (solid) has a slope of 1.11 (48°). At 5 s the modeled mean period is 0.18 s low and at 10 s it is 0.37 s high.

[63] The modeled and observed mean wave direction (from) are compared in Figures 6 and 7. They show good

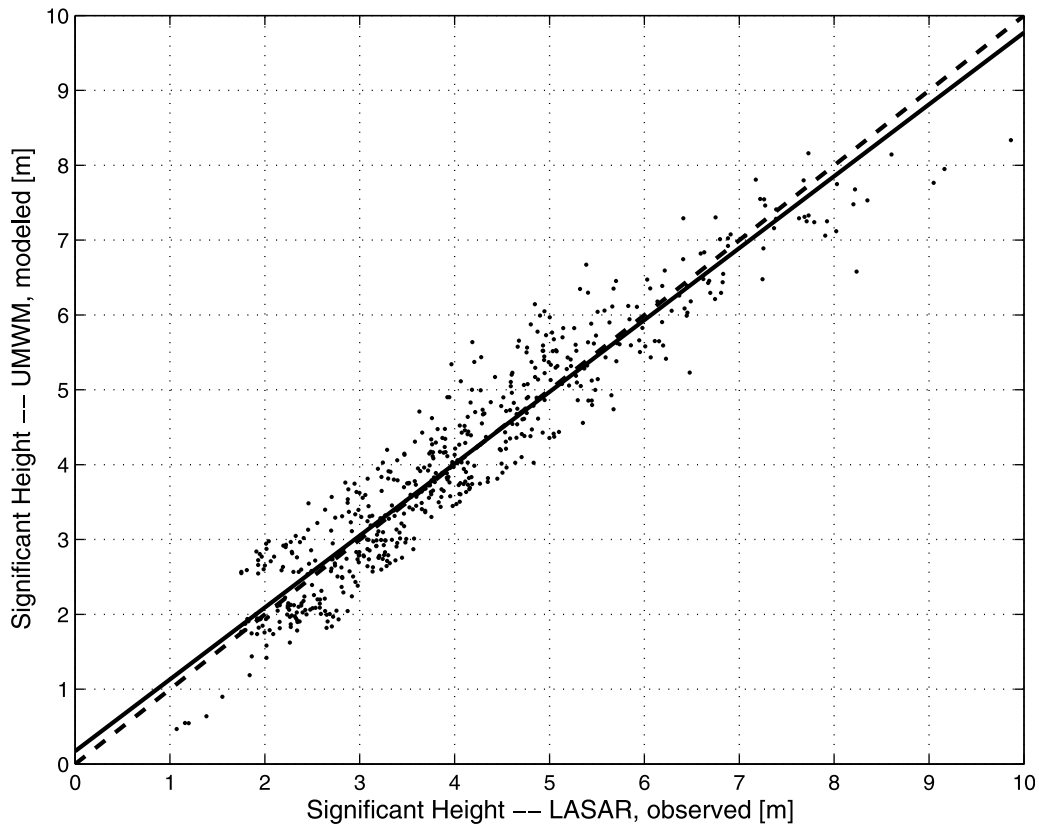


Figure 3. Comparison of modeled (UMWM) and observed (LASAR) significant heights. The 45° agreement line (dashed) and the least squares regression line (solid) are shown.

agreement even in rapidly changing directions. In Figure 8 we compare the modeled (Figure 8, top) and observed (Figure 8, middle) frequency-direction spectra for two cases: (1) changing wind direction and moderate significant height (Figure 8, left) and (2) steady wind direction and large significant height (Figure 8, right). The heavy black bar at the center of the polar diagrams indicates the modeled mean wind speed and direction (to). Figure 8 (bottom) shows the corresponding scaled frequency spectra (modeled, red; observed, black) and the directional spread (modeled, blue; observed, green) in each frequency bin. The directional spread is defined as twice the standard deviation of direction about the mean direction or twice the square root of the second directional moment of the directional energy spectrum divided by the zeroth moment. Both modeled and observed spreads have the same pattern in the energy containing regions of the spectra, i.e., from $0.5f_p$ to $2.5f_p$. Around the peak the spectral width is about 40° , widening rapidly to lower frequencies and more slowly to higher frequencies to about 60° by $2f_p$. At even higher frequencies the modeled spectra do not widen appreciably, while the observed spectra continue to widen. Probable causes for this include: the wind directional variability on shorter times than the 3 h averaged winds supplied to the wave model; scattering from nearby structures of the shorter waves.

3.2. The Source Function Balance

[64] To examine the source function balance at short fetch and at full development we ran UMWM with constant wind

($U_{10} = 15$ m/s) directed along the length of a rectangular basin $300 \text{ km} \times 60 \text{ km}$. The model was evolved for 60,000 s so that the waves would not be duration limited but rather were fetch limited at short fetch and fully developed at long fetch. Figures 9 and 10 show the source/sink functions and the spectra along a 30° slice in the wind direction for fetch-limited ($fetch = 12 \text{ km}$, $U/C_p = 1.87$) and nearly fully developed ($fetch = 264 \text{ km}$, $U/C_p = 1.08$) cases respectively. The spectra and source functions are multiplied by wave number, k and plotted against the logarithm of k so that the area under the curve is proportional to variance. The drag coefficient, C_d and the inverse wave age, U/C_p are shown versus fetch along the centerline of the basin. As the waves develop U/C_p decreases from 1.87 at short fetch, asymptotically approaching 1 at full development. As the peak waves approach the wind speed, the drag coefficient relaxes from 0.00163 at short fetch to 0.00159 at full development.

[65] The spectra and source functions in Figure 9 are characteristic of fetch limited conditions. The spectra at fetch of 24 km (open circles) show the rapid development with fetch. Energy increase is largely on the peak and forward face, while the equilibrium range remains essentially unchanged. The wind input source function, S_{in} at short fetch is centered slightly to the right of the peak and is much broader than the spectrum (asterisks) with strong inputs on the forward face and the equilibrium range. S_{ds} , the wave breaking dissipation function (asterisks) covers the same wave number range as S_{in} , but is about half as large. S_{dt} , dissipation by ambient turbulence (open circles) is proportional to k times

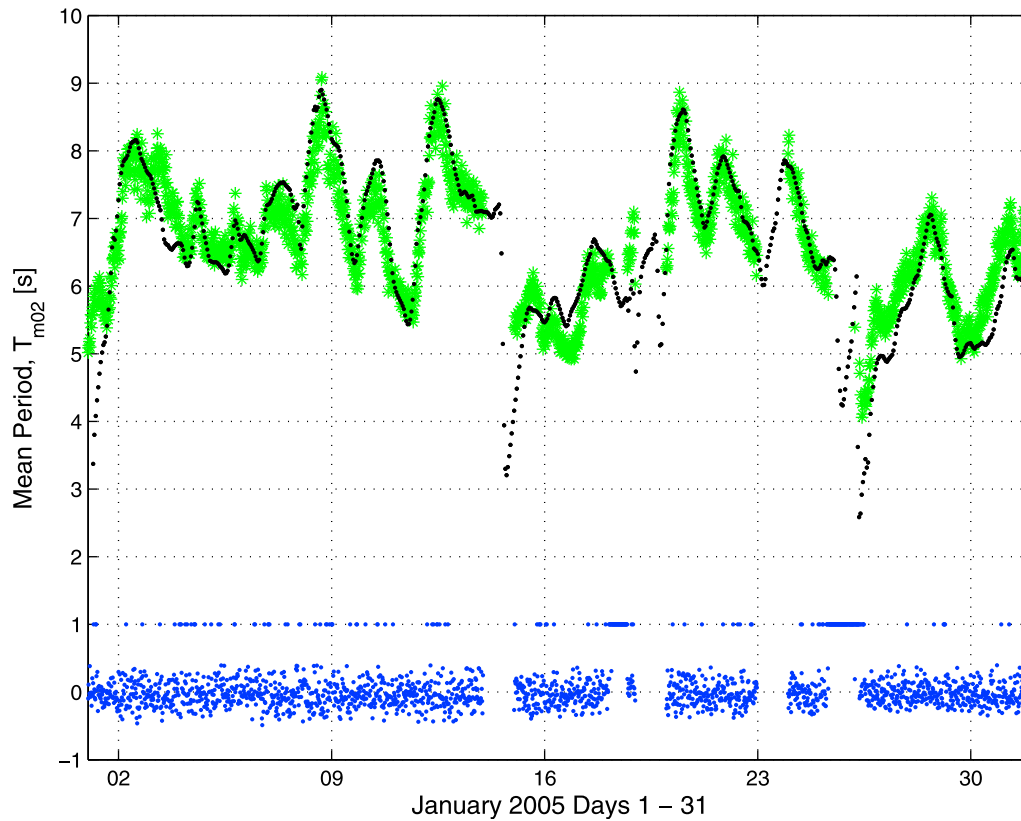


Figure 4. Time series of observed (green asterisks) and modeled (black dots) mean period, T_{m02} , at Ekofisk, January 2005. The observations were made with LASAR, an array of laser range finders on the corners of a square of side 2.6 m. The blue dots are the kurtosis -3 of the surface elevation observations; values greater than 0.4 are not used in the regression analysis in Figure 5.

the spectrum, so it is broader than the spectrum and slightly shifted toward higher wave numbers. S_{nl} , the nonlinear source function moves energy from the equilibrium range to the peak and forward face. The net source function has a single positive lobe centered on the spectral peak. From $4.6k_p$ up the net source function is essentially zero.

[66] The spectra and source functions in Figure 10 are characteristic of nearly fully developed conditions, $U/C_p = 1.08$. The spectrum at 12 km larger fetch (open circles) is essentially unchanged. The net source function has a single lobe centered on the forward face of the spectrum. The corresponding growth over 12 km is negligible; for all practical purposes the waves, generated by a 15 m/s wind, have reached full development at 264 km fetch. The wind input source function is centered on the equilibrium range at $3k_p$. There is very little wind input at the peak. S_{ds} , the wave breaking dissipation function is about two thirds as large as S_{in} and is shifted toward the peak; it is centered on $2.4k_p$. There is occasional breaking of the waves at the spectral peak. S_{nl} , the nonlinear source function moves energy from the equilibrium range to the peak and forward face as at short fetch, but the amount transferred, relative to the spectral density, is less than 15% of that transferred in the short fetch case.

3.3. Modeling the Wind Stress

[67] The momentum transferred from atmosphere to waves and currents is calculated in UMWM as described in section 2.3.2. UMWM was run on a $300 \text{ km} \times 60 \text{ km}$ basin for 60,000 s with uniform steady winds at 10 m height as input. The resulting drag coefficients and inverse wave ages at fetch of 276 km are graphed in Figure 11. Below 10 m/s the waves are fully developed, or nonexistent below 2 m/s. The drag coefficient (C_d) is a minimum (0.001) at 2 m/s. By 3 m/s waves begin to form and C_d increases as form drag contributes to the mix. By 6 m/s, where whitecaps first appear, form and skin drag are balanced (Figure 12) and C_d increases sharply with wind speed in much the same manner as in the field measurements of *Large and Pond* [1981] and *Geernaert et al.* [1987]. Beyond 25 m/s the rate of increase of C_d with wind speed relaxes somewhat reaching 0.0027 at 55 m/s, a little above the limiting value of 0.0025 found by *Donelan et al.* [2004] in laboratory experiments. Drag coefficient measurements on the open ocean are seldom accompanied by wave measurements, but the limited fetch determined by storm size yields a positive correlation between U/C_p and U_{10} .

[68] We remark that the successful modeling of the drag coefficient confirms the choice of A_1 , the proportionality constant in the wind input source function.

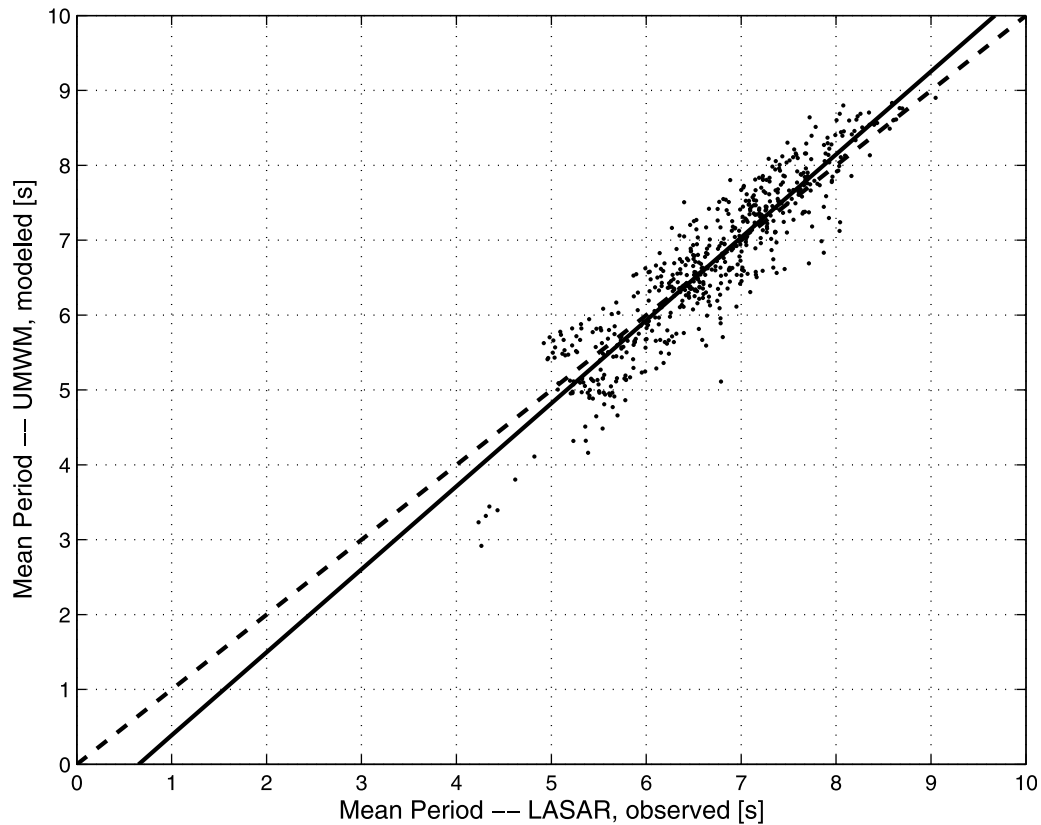


Figure 5. Comparison of modeled (UMWM) and observed (LASAR) mean periods. The 45° agreement line (dashed) and the least squares regression line (solid) are shown.

[69] The need for an accurate and fast wave and stress model is underscored in Figure 12, where it is shown that form (wave) drag dominates the atmosphere–ocean coupling above 6 m/s and rises to 90% of the total drag in very strong winds.

4. Spectral Shape Tests With Hindcast Winds in Hurricane Bonnie (1998)

[70] After the source function proportionality coefficients have been determined in the previous section, we apply the wave model to a hurricane case, and compare the results with observations. Hurricanes in the open ocean are a good test case for evaluating the performance of a wave model because the wavefield in hurricanes is very complex. In order to predict integral wave quantities inside the storm and in the environment, correct representation of the full wave number–directional spectrum is necessary. Furthermore, it is established that ocean waves play an important role in momentum transfer between winds and ocean currents [Fan *et al.*, 2009, 2010].

[71] Wind speeds range from very high (>50 m/s) in the inner core of the storm, to low (<10 m/s) in the environment. In addition, the storm moves over the ocean, generating complex, asymmetric wavefields. The waves on the right-hand side of the storm propagate with the storm, thus experiencing longer fetch and correspondingly more energetic wind sea. In the right front quadrant swell generated in

an area on the right side and toward the rear of the storm will be mixed with the wind sea. The variance spectrum in this region is usually broad and sometimes bimodal. The wind sea is approximately in the direction of the local wind. These waves grow longer and higher, and eventually radiate away from the storm when their group velocity exceeds the storm translation velocity. The swell waves leave the storm and enter the environment where they are subject to slow attenuation in low-wind conditions.

[72] The wind sea on the left-hand side of the storm experiences shorter fetch, as it propagates against the direction of storm translation, and is consequently less developed. The swell that has been generated in an area on the right side of the storm now propagates across the wind, experiencing little attenuation. Thus, the variance spectrum in this region is usually broad with a strong swell peak propagating in a direction clockwise from the wind and skewed at shorter wavelengths toward the wind direction. In general, waves on the left side of the storm are noticeably lower because wind sea in the direction of the local wind experiences a shorter fetch. The wavefield gets more complicated as the storm changes direction or translation speed, enters intermediate or shallow water, or crosses areas of sharp current gradient.

[73] Observations of directional wave spectra in hurricane conditions have been obtained from a joint effort between NASA/Goddard Space Flight Center/Laboratory for Hydro-spheric Processes and NOAA/AOML/HRD. The data were obtained during Hurricane Bonnie in August 1998 by the

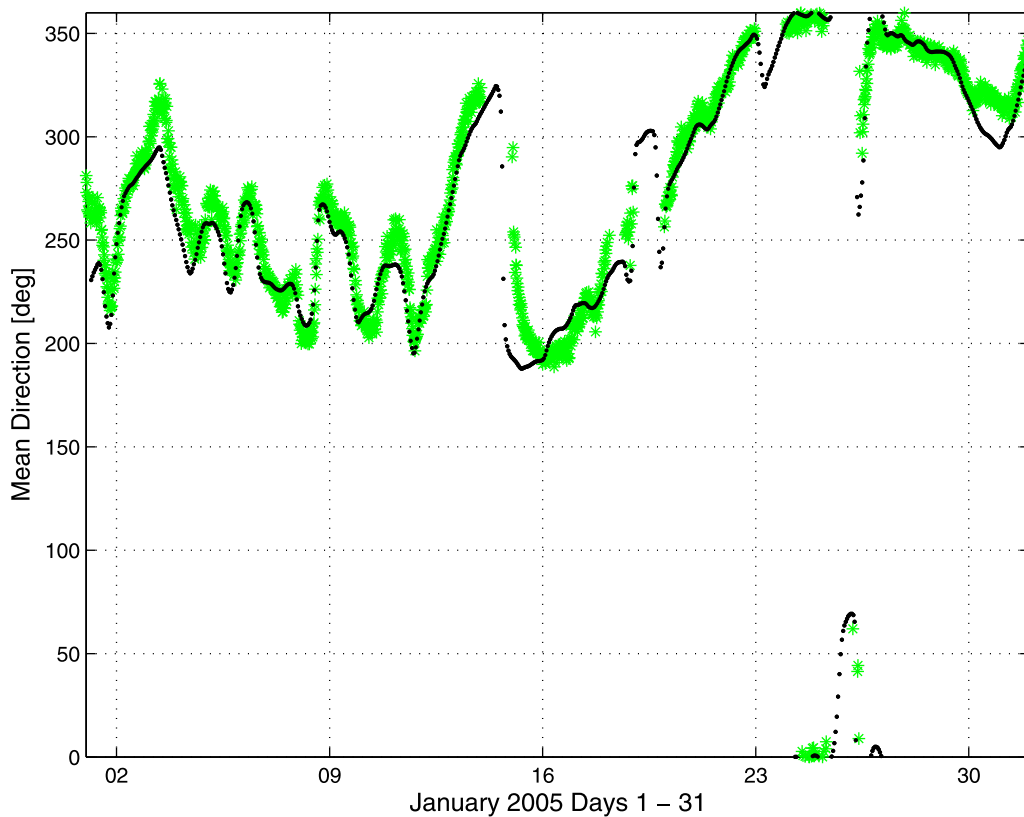


Figure 6. Time series of observed (green asterisks) and modeled (black dots) mean direction at Ekofisk, January 2005. The observations were made with LASAR, an array of laser range finders on the corners of a square of side 2.6 m.

NASA airborne scanning radar altimeter (SRA) mounted aboard a NOAA hurricane research aircraft. These measurements and their processing were described in detail by *Wright et al.* [2001] and *Walsh et al.* [2002]. They were recorded during two flights, in the open ocean on 24 August 1998 and near landfall on 26 August 1998. We use the data set from the open ocean (24 August) to evaluate the performance of the wave model inside Hurricane Bonnie (1998).

[74] The wave model was set up for simulation of wavefields forced by Hurricane Bonnie winds from 22 to 28 August 1998. High-resolution wind forcing was provided by University of Miami Coupled Model (UMCM), described in *Chen et al.* [2007]. The components of UMCM are the Fifth Generation Penn State University/National Center for Atmospheric Research nonhydrostatic mesoscale model (MM5) [Dudhia, 1993] for the atmosphere, NOAA/NCEP Wavewatch III [Tolman, 1991] for the ocean waves, and 3DPWP [Price et al., 1986] for the ocean. UMCM has a parent domain, with horizontal grid resolution of 45 km, and three nested domains of 15, 5, and 1.67 km horizontal grid resolution each. Grid size of the parent domain is 150 by 120 grid cells, 121 by 121 for 15 and 5 km nests, and 151 by 151 for the innermost nest. The two innermost domains are moving, vortex-following domains. The wave model domain in this study was set up on a Cartesian grid of 478 by 478 cells, with horizontal resolution of 5 km. The spectral resolution consisted of 25 logarithmically spaced frequency bins in the range of 0.0313–0.5 Hz, and 36 directional bins ($\Delta\phi = 10^\circ$). The wind forcing from UMCM at this

resolution also contains information interpolated from the innermost domain (1.67 km). The wave model (UMWM) was run (uncoupled) with these winds and currents computed by 3DPWP ocean model. Bathymetry was provided by NOAA/National Geophysical Data Center ETOPO1 1 Arc-Minute Global Relief Model [Amante and Eakins, 2009]. The model was initiated from a calm state. Both modeled storm track and intensity are in reasonable agreement with observed ones. However, the modeled storm track was off in the period between 23 and 26 August, and also it propagated faster than the observed storm. During the mature storm stage (24–26 August), the modeled intensity was higher by 10 to 20% on average. Because of these shortcomings in the hindcast wind field on 24 August, we cannot make a quantitative comparison of wave heights and periods with the SRA. Instead we compare the spectral shapes observed by the SRA with those calculated by the UMWM in the four quadrants of the storm. (A quantitative comparison of spectral properties against NDBC buoys is made in the next section.)

[75] We compare the spectral shapes in the four quadrants with respect to the north-northwestward translating eye (front left; front right; rear right; rear left; going clockwise from Figures 13 (top left) and 14 (top left)). The typical hurricane pattern is apparent in both figures: larger waves on the right side than on the left and at the front quadrants compared with the rear quadrants. The modeled spectra (Figure 14) show a distinct combination of swell and wind sea. The swell, generated over an area 45° – 90° clockwise

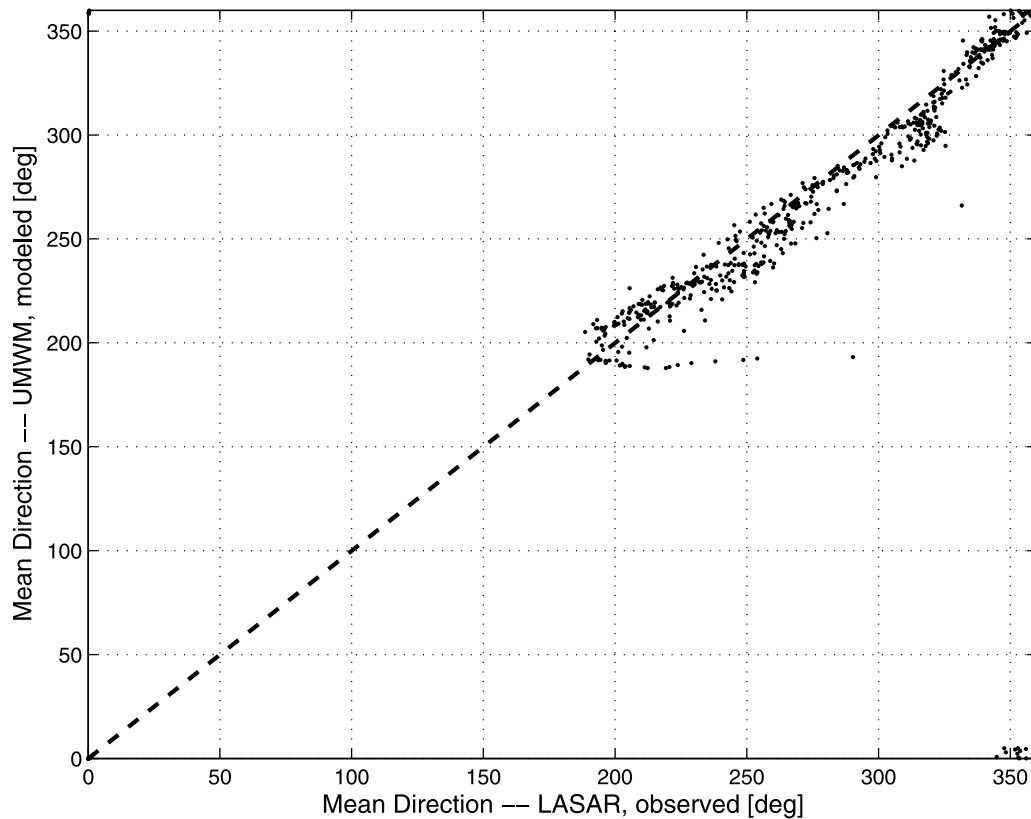


Figure 7. Comparison of modeled (UMWM) and observed (LASAR) mean directions. The 45° agreement line (dashed) is shown.

from the location of the spectrum, is dominant. On the right side of the storm the wind sea is enhanced, by the translation of the storm in the wind direction, and it appears as a broad counterclockwise skewness of the spectrum or even a bimodal spectrum in the rear right quadrant. On the left side of the storm the wind sea is less developed due to the reduced fetch for wind sea propagating against the translation of the storm. The local wind sea peak is apparently less than 20% of the swell peak and barely shows up in the wind direction. The significant heights are larger on the right side of the storm than on the left. Generally, these features appear in the SRA spectra (Figure 13) and the UMWM spectra (Figure 14) although the skewness of the spectra toward the wind direction in the front quadrants is not as pronounced as in the UMWM spectra. Both systems show broad multimodal spectra in the right rear quadrant.

5. Simulation of Waves Using Analyzed Winds in Hurricane Ike (2008)

[76] We now apply the model to simulate waves under Hurricane Ike (2008). We chose this storm for three main reasons: High availability of analyzed surface wind data (HWIND) derived from flight observations by NOAA-HRD [Powell *et al.*, 1998]; High availability of wave and wind observations from NOAA-NDBC (National Data Buoy Center) stations; Hurricane Ike was a very intense storm with peak wind speeds of 63 m/s, which induced significant wave heights of over 10 m, and we find it a good test case for validating a wave model.

[77] The HWIND data for Hurricane Ike was available in almost regular 3-hourly intervals for the period between 8 and 13 September 2008. During this period, the storm was moving from Cuba, over the Gulf of Mexico, to the coast of Texas where it made its second landfall. Because the HWIND data set covers limited area around the storm, we merge this data set with GFS (Global Forecast System) forecast wind fields. The two data sets are interpolated in time (hourly) and in space (4 km horizontal resolution) in order to provide a uniform wind forcing for the wave model. This way, we remove the uncertainty coming from possible errors in hurricane track and translation speed.

[78] UMWM was set up on a 4 km horizontal resolution in Cartesian projection, with domain size of 898 by 688 grid cells. We chose this higher horizontal resolution in order to minimize errors due to bottom topography. As for the Hurricane Bonnie case, described in the previous section, the bottom topography data was provided by NOAA-NGDC ETOPO1 1 Arc-Minute Global Relief Model. The spectral resolution of the model was 37 frequency bins in the range of 0.0313–2 Hz, and 36 directional bins. We initialize the model from a calm state at 12:00 UTC on 8 September 2008 and finalize it at 12:00 UTC on 13 September 2008.

[79] The wave model domain and Hurricane Ike track are shown in Figure 15. We compare the simulated significant wave height and mean wave period with measurements recorded at NOAA-NDBC stations 42001, 42002, 42007 and 42039. Buoy locations are marked with a plus symbol. We chose these four locations because they are representative for wavefields inside the storm (42001), outside the

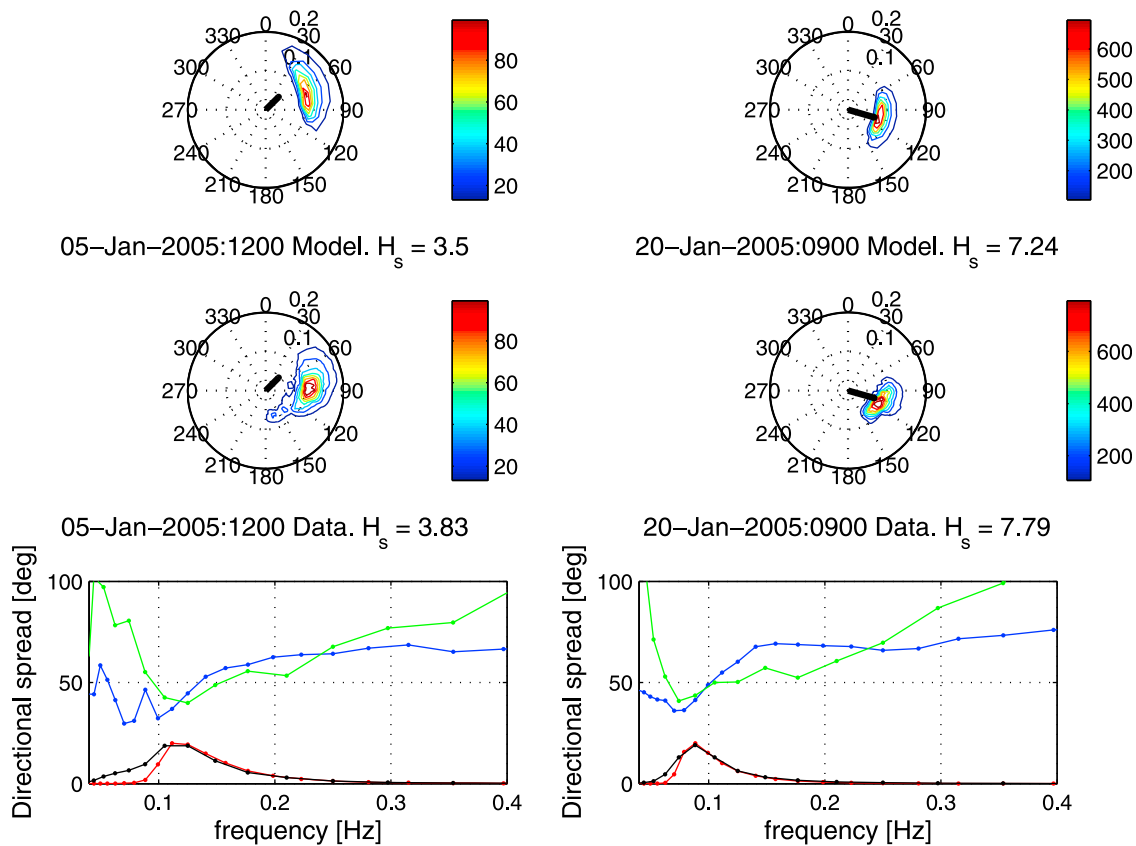


Figure 8. Comparison of directional spectra (top) modeled with (middle) observed. (bottom) The frequency spectra (modeled, red; observed, black) and directional spread (modeled, blue; observed, green).

storm on the left-hand side (42002) and right-hand side (42039), and in shallow water (42007).

[80] Figures 16–19 show the comparison of significant wave height, mean wave period, and wind speed between model simulations and NDBC buoy measurements. Two model simulations are shown on each figure, one for bottom friction (G_f) and percolation (G_p) coefficients values of 0.001 m/s, and the other for values of 0.01 m/s. We chose to show these two cases because the choice of values for these two coefficients is important for correctly simulating waves in shallow water (i.e., station 42007, water depth of 14.9 m). Results shown in Figure 18 suggest that the correct values for G_f and G_p lie somewhere between 0.001 and 0.01 m/s.

[81] The results in deep water locations are overall in good agreement with observations. At times when analyzed surface winds are overestimated by 20% to 30% (i.e., station 42001 between hours 72 and 96), wave heights and mean period are overestimated also, as expected. All four locations show a delay in mean wave period growth during the first 48 to 72 h. This happens for two reasons. First, the model is initiated from a calm state, and it takes around 24 h for the full spectrum to develop. Second, some swell waves which originated from the storm at the time before 12:00 UTC, 8 September, do not exist in the model, but they do in reality, as it is recorded by NDBC stations. Thus, model results are not representative for comparison during this period.

[82] Figure 20 shows the significant wave height (color) and mean wave direction (vectors), at 06:00 UTC on 12 September 2008, when the storm exhibited strong sustained

winds for several hours. The thick black arrow indicates the direction of storm translation. Highest swell waves (up to 20 m) that propagate in the same direction are on the right-hand side of the storm. The asymmetry in the significant wave height fields comes from the storm translation which creates longer effective fetch on the right-hand side and shorter on the left-hand side. Near the coast, there is evidence of bottom induced wave refraction and shoaling.

[83] Figure 21 shows the drag coefficient scatter as function of wind speed, for the same time as for Figure 20. We make a distinction between points in shallow water (depth less than 30 m) and deep water (depth larger than 30 m). Shallow water points exhibit higher drag coefficients for same wind speed, because the waves of the same frequency are slower and shorter and consequently steeper, thus producing higher stress. Most points are in range of measured values by *Geernaert et al.* [1987] and *Large and Pond* [1981], and slightly level off with increasing wind speed.

6. Summary

[84] A full spectral model for wave and wind stress prediction has been developed. The model is based on the energy balance equation forced by seven source/sink functions. These functions mimic the main physical processes that affect the evolution of surface waves in liquids of arbitrary depth. Their forms are based on theory and field and laboratory experiments and their magnitudes are determined by comparison of modeled and observed data. In deep

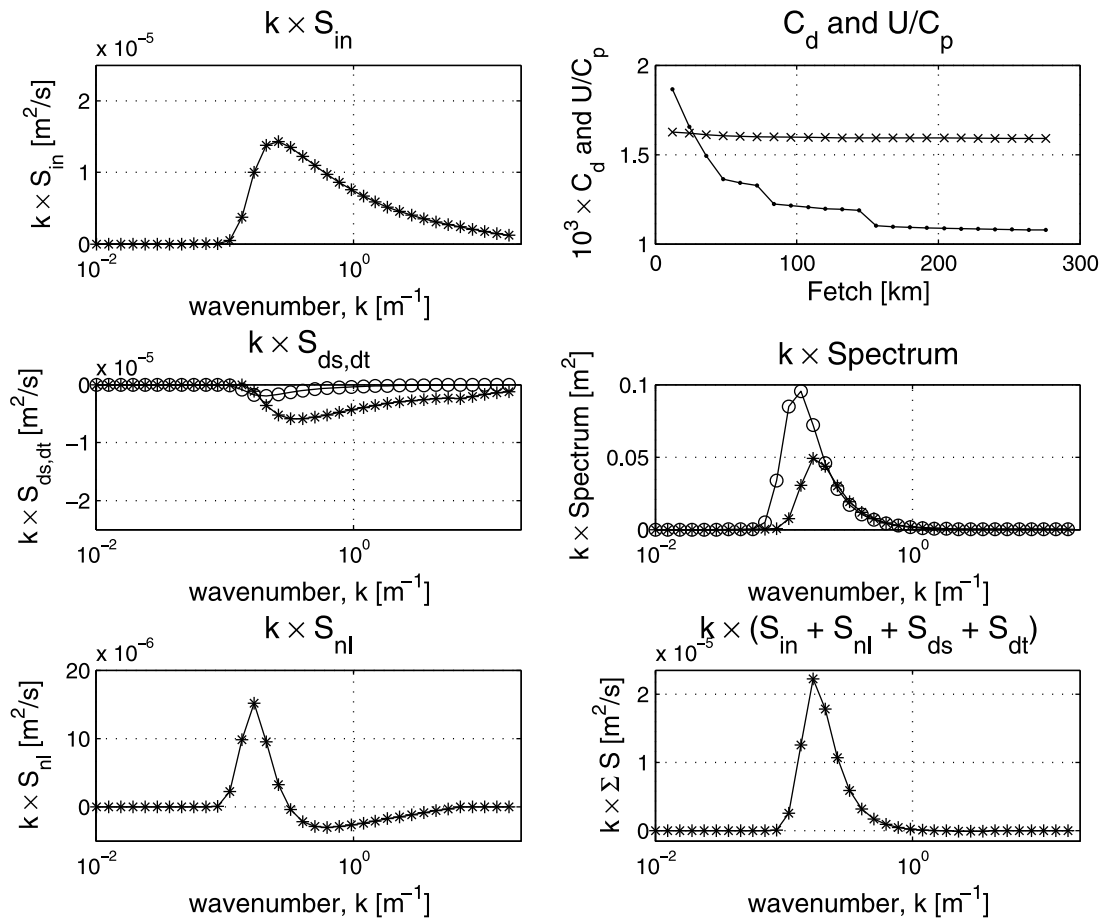


Figure 9. Source functions and spectrum at short fetch of 12 km in a 15 m/s wind. The spectrum at 24 km fetch and S_{dt} , the sink function due to turbulence, are shown (open circles). The fetch dependencies of C_d and U/C_p are indicated by crosses and dots, respectively.

water the principal source functions are: energy input from the wind; dissipation through wave breaking; dissipation due to turbulence; nonlinear interactions. The wind provides the only energy source and in a growing wind sea it is the largest source function and is distributed over all waves traveling slower than the wind. The principal sink function is the dissipation of spilling breakers (whitecaps). It is smaller (50% to 70%) than the wind input at their respective peaks, but is somewhat broader. Turbulence in the water column provides additional dissipation through the interaction of turbulent eddies with the wave orbital velocity structure. It is typically less than 20% of the whitecapping dissipation. The nonlinear source/sink function is conservative and moves energy from the equilibrium range to longer waves at the peak and on the forward face of the spectrum. The nonlinear transfer enables the development of the spectrum by moving energy to longer waves than the peak, whence they can interact with the wind. All other source functions are proportional to the spectrum and so, on their own, cannot produce the observed evolution of wind sea spectra. Therefore, comparison with data provides a sensitive quantification of the nonlinear source function.

[85] An array of laser range finders in the Ekofisk oil field provided an excellent opportunity to calibrate the source functions in the North Sea using carefully analyzed winds.

The calibration factors for each source function were fixed by optimizing the comparisons of modeled and observed significant height and mean period. The wind input calibration factor (the sheltering coefficient) enters the calculation of form (or wave) stress. Sheltering alters the surface area exposed to flow, and hence the skin stress. The modified skin stress and the form stress are summed vectorially and the resulting total drag coefficient is shown to have the observed structure versus wind speed. In the energy containing region the modeled and observed spectra and directional spreads are in good agreement. This further confirms the wind input source function, the only source function with explicit directional dependence.

[86] Form stress exceeds skin stress at wind speeds in excess of 6 m/s, and rises to almost 90% of the total stress in very strong winds. Some of the form stress goes to increase wave momentum and the rest drives the surface currents. Appropriate separation of these two stresses requires an accurate wave model. This emphasizes the need for wave and stress modeling in coupling atmosphere and oceans.

[87] The calibrated model (UMWM) is exercised with a modeled wind field for 5 days of Hurricane Ike (2008). Comparisons with NDBC buoys, in deep and shallow water, show good agreement with some discrepancies where modeled winds did not match the buoy observations.

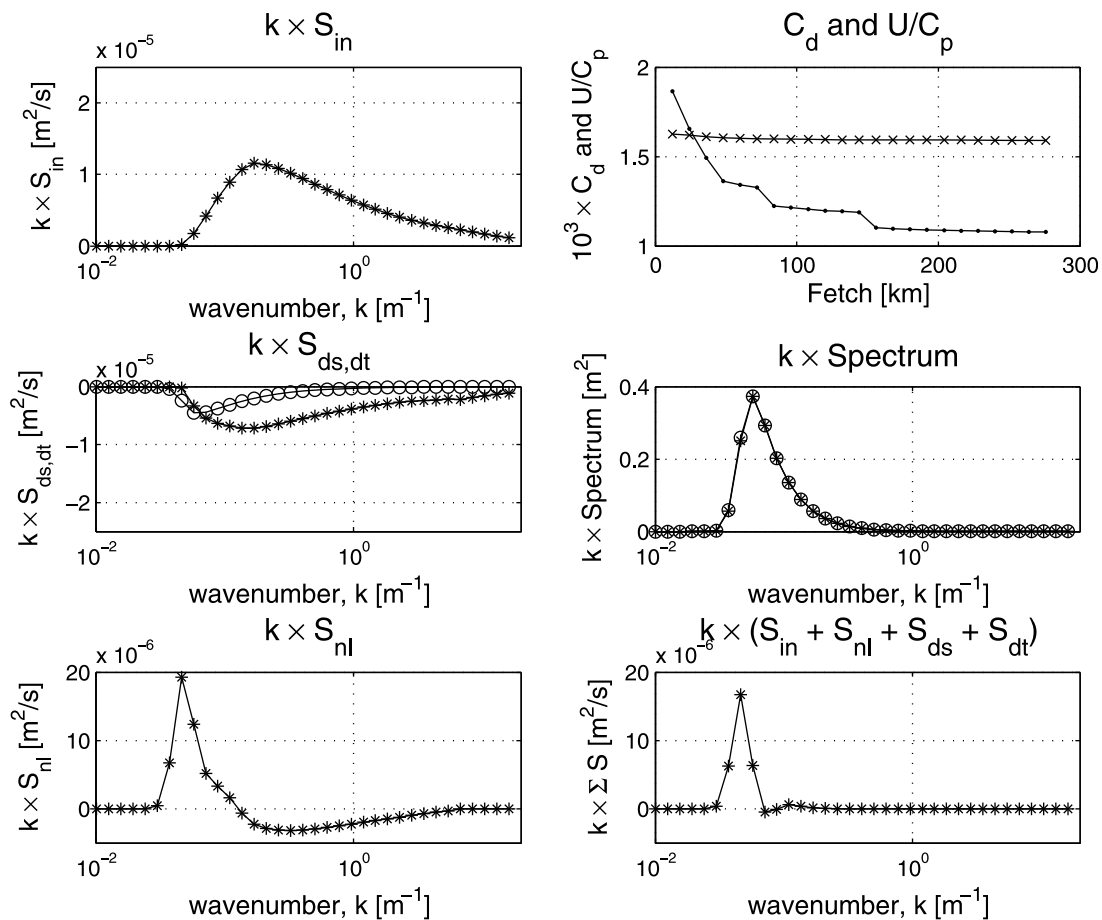


Figure 10. Source functions and spectrum at long fetch of 264 km in a 15 m/s wind. The spectrum at 276 k fetch and S_{dt} , the sink function due to turbulence, are shown (open circles). As in Figure 9, the fetch dependencies of C_d and U/C_p are indicated by crosses and dots, respectively.

Aircraft wave number spectra were used to verify the spectral shape of the mixed seas in the four quadrants around the eye of Hurricane Bonnie (1998).

[88] Finally, the drag coefficients in deep and shallow water were calculated and shown to depend on wave age of the wind sea, on propagation direction of swell with respect to the wind, and on water depth. This further underscores the need for wave and stress modeling in coupling atmosphere and ocean in strong winds.

[89] Physically based, full coupling among winds, waves, and currents requires a wave model to have the capability and flexibility of incorporating wind-wave and wave-current coupling physics that is energetically consistent across the air-sea interface. The formulation of UMWM is designed with these new applications in mind. It is more flexible in implementing new coupling physics than other existing wave models.

[90] Computationally simple physics and propagation schemes make UMWM a robust and efficient wave model. UMWM takes advantage of parallel processing, and scales well on more than 200 processors. In addition, its design follows the standard of the Earth System Modeling Framework (ESMF) [Hill *et al.*, 2004], which makes it suitable for coupling to atmosphere and ocean circulation models.

UMWM source code and its user manual are available at <http://rsmas.miami.edu/groups/umwm>.

Appendix A: Spatial Discretization

[91] The time evolution of the variance spectrum due to advection in Cartesian projection is given by

$$\frac{\partial E}{\partial t} = -\frac{\partial[(c_g \cos \phi + u)E]}{\partial x} - \frac{\partial[(c_g \sin \phi + v)E]}{\partial y} - \frac{\partial(\dot{\phi}E)}{\partial \phi} \quad (\text{A1})$$

where u and v are ocean current components in x and y , respectively, and $\dot{\phi}$ is the rotation rate. Both geographical propagation and refraction terms are discretized using first-order upstream differencing. This scheme is positive-definite, quantity conserving, implicitly diffusive and computationally efficient. We believe that conserving the shape and integral of the simulated quantity is more important than the formal order of accuracy of the scheme. A certain amount of diffusion is desirable in order to avoid swell separation between discrete directional and frequency bins. In the event where swell separation would become apparent (e.g., in larger basin-scale simulations), directional and frequency resolution would have to be increased to alleviate this effect.

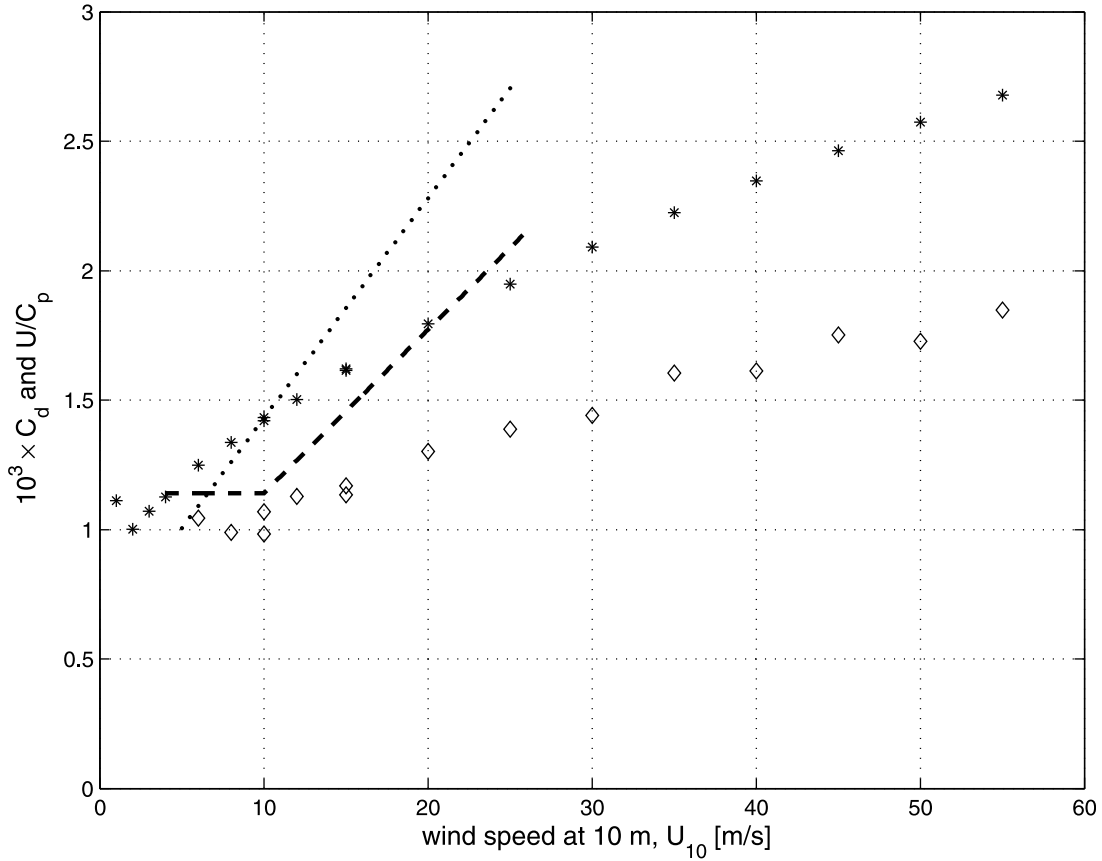


Figure 11. The modeled drag coefficient at 276 km fetch, C_d (asterisks), referred to 10 m height versus wind speed, U_{10} . The dashed and dotted lines represent the observations of *Large and Pond* [1981] and *Geernaert et al.* [1987], respectively. The inverse wave age, U/C_p (diamonds) shows that the waves at 276 km fetch are well developed at low winds and increasingly fetch limited as the wind speed increases.

[92] A spatial differencing operator is discretized as:

$$\frac{\partial(\dot{x}E)}{\partial x} \approx \frac{\Phi_{i+1/2} - \Phi_{i-1/2}}{\Delta x} \quad (\text{A2})$$

where i is a discrete index along dimension x . Fluxes at cell edges $\Phi_{i+1/2}$ and $\Phi_{i-1/2}$ are defined as:

$$\Phi_{i+1/2} = \frac{\dot{x}_{i+1/2} + |\dot{x}_{i+1/2}|}{2} E_i + \frac{\dot{x}_{i+1/2} - |\dot{x}_{i+1/2}|}{2} E_{i+1} \quad (\text{A3})$$

$$\Phi_{i-1/2} = \frac{\dot{x}_{i-1/2} + |\dot{x}_{i-1/2}|}{2} E_{i-1} + \frac{\dot{x}_{i-1/2} - |\dot{x}_{i-1/2}|}{2} E_i \quad (\text{A4})$$

and

$$\dot{x}_{i\pm 1/2} = \frac{\dot{x}_i + \dot{x}_{i\pm 1}}{2} \quad (\text{A5})$$

The above treatment of flux differencing ensures upstream definiteness.

[93] For propagation in two-dimensional space, the stability of the scheme is ensured for:

$$\mu = \frac{\dot{x}\Delta t}{\min(\Delta x, \Delta y)} < \frac{1}{\sqrt{2}} \quad (\text{A6})$$

where μ is the Courant number. Depending on the choice of number of directional bins, the stability criterion is more permissive:

$$\mu = \frac{\dot{x}\Delta t}{\min(\Delta x, \Delta y)} < \cos\left(\frac{\pi}{4} - \frac{\Delta\phi}{2}\right) \quad (\text{A7})$$

where $\Delta\phi$ is the directional bin size. The criterion (A7) is satisfied if the number of directional bins is divisible by 8.

[94] For ocean grid cells next to the land or domain edges, an open boundary condition is applied; that is, energy can freely propagate into land. It is assumed that the coast is absorptive for all energy that has not been dissipated in the surf zone. In the case of global domain simulation, periodic boundary conditions are applied at east and west domain edges.

[95] The rotation rate $\dot{\phi}$ in the refraction term is evaluated as vorticity of phase velocity modulated by currents:

$$\dot{\phi} = \frac{\partial(c \sin\phi + v)}{\partial x} - \frac{\partial(c \cos\phi + u)}{\partial y} \quad (\text{A8})$$

The change due to refraction is then computed using (A1)–(A5). Positive and negative values of $\dot{\phi}$ correspond to counterclockwise and clockwise rotation of energy, respectively. The stability constraint for the refraction term is the

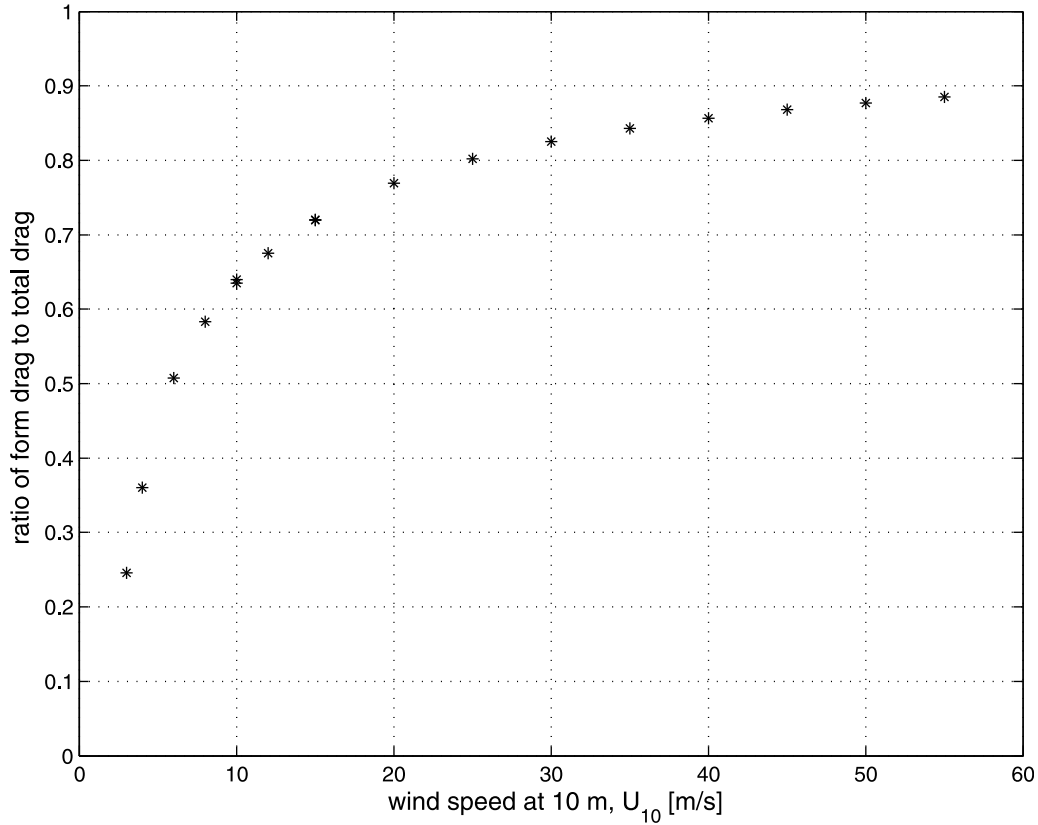


Figure 12. The ratio of form drag to total drag versus wind speed at 10 m, U_{10} .

same as for one-dimensional advection:

$$\mu = \frac{\dot{\phi} \Delta t}{\Delta \phi} < 1 \quad (\text{A9})$$

For most domain cells, the allowed refraction time step is larger than the advective step given in (A7). In case that condition (A9) is violated, which may occur on sharp bathymetric or current gradients, the rotation at these points is limited so that $\mu = 1$. This affects the solution insignificantly, while maintaining computational efficiency. Because the domain is periodic in directional space, there is no need for boundary conditions.

[96] A more detailed discussion about the advection scheme presented here, as well as rationale for using it in wave modeling, can be found in a review paper by *Cavaleri et al.* [2007].

Appendix B: Time Discretization

[97] Once all the source terms in (1) have been evaluated, $E(k, \phi)$ is integrated forward in time. We evaluate the contribution from source and advection terms separately:

$$\frac{\partial E}{\partial t} = \left(\frac{\partial E}{\partial t} \right)_s + \left(\frac{\partial E}{\partial t} \right)_a \quad (\text{B1})$$

The contribution from source terms can be written as:

$$\left(\frac{\partial E}{\partial t} \right)_s = \sum_{i=1}^n S_i^* E \quad (\text{B2})$$

where S_i^* is just S_i/E . Then, by integrating (B2) over a finite time interval Δt , a solution is available in the form of:

$$E_s^{n+1} = E^n \exp \left(\sum_{i=1}^n S_i^* \Delta t \right) \quad (\text{B3})$$

[98] The time increment Δt is dynamically computed so that the variance spectrum E can only grow by a pre-determined, finite factor:

$$\frac{E_s^{n+1}}{E^n} = \exp \left(\sum_{i=1}^n S_i^* \Delta t \right) < r \quad (\text{B4})$$

where r is usually set between 1.5 and 2. Lower values of r will draw E closer to the solution attractor.

[99] Then, a time-splitting approach is used to achieve a more stable integration:

$$E^* = \frac{E^n + E_s^{n+1}}{2} \quad (\text{B5})$$

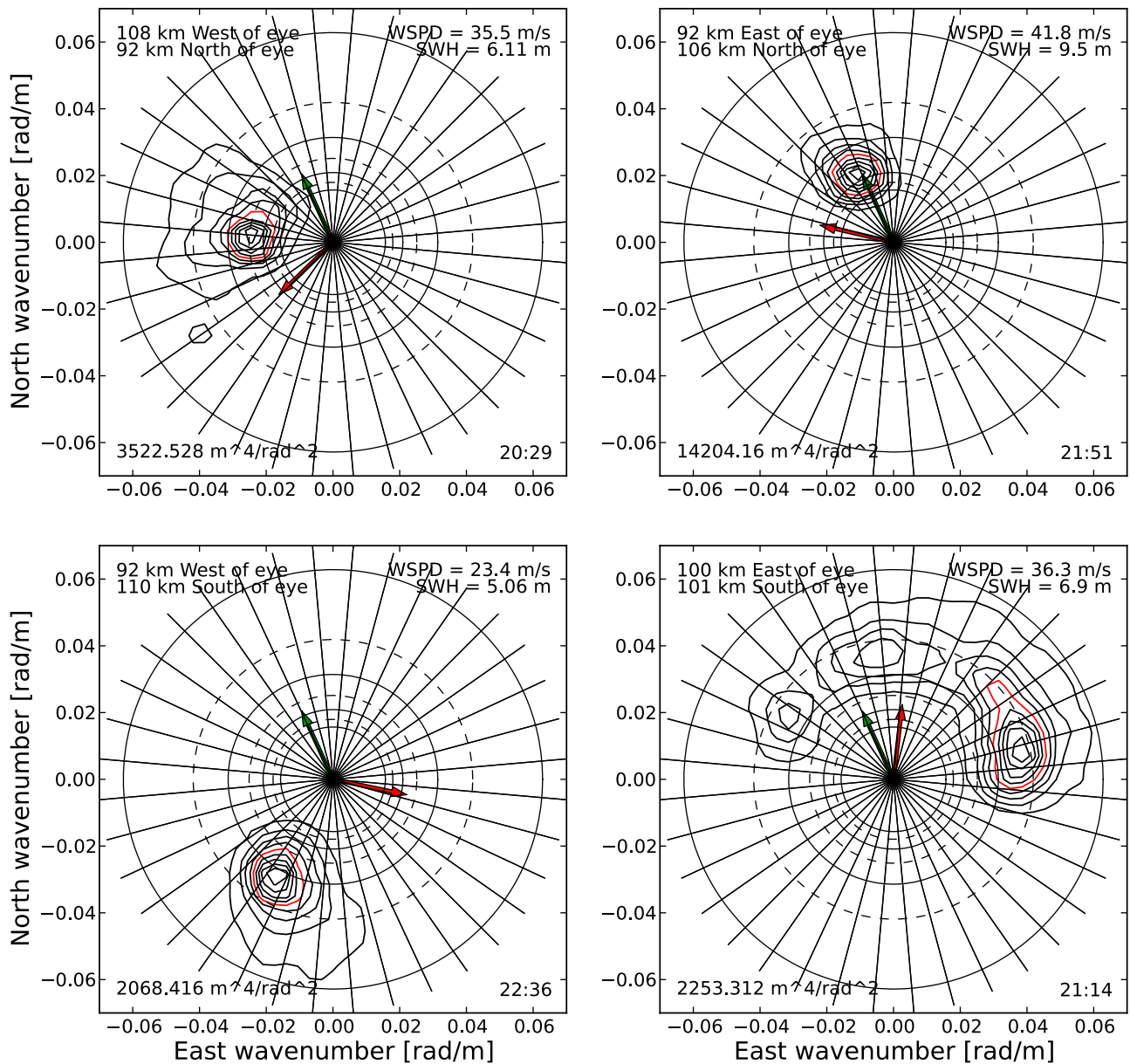


Figure 13. Observed variance spectrum by SRA at four locations around the storm on 24 August 1998. Location relative to storm center is indicated in the top left corner. Contours are drawn for each tenth percentile of the spectrum peak. The 50% contour is indicated in red. Spectrum peak value is given in the bottom left corner. Circles mark 100, 150, 200, 250, 300, 350, and 400 m wavelengths, from outside toward the center. Wind speed and significant wave height are shown in the top right corner. Approximate time of measurements is given in the bottom right corner. Red and green arrows show directions of local wind and storm translation, respectively.

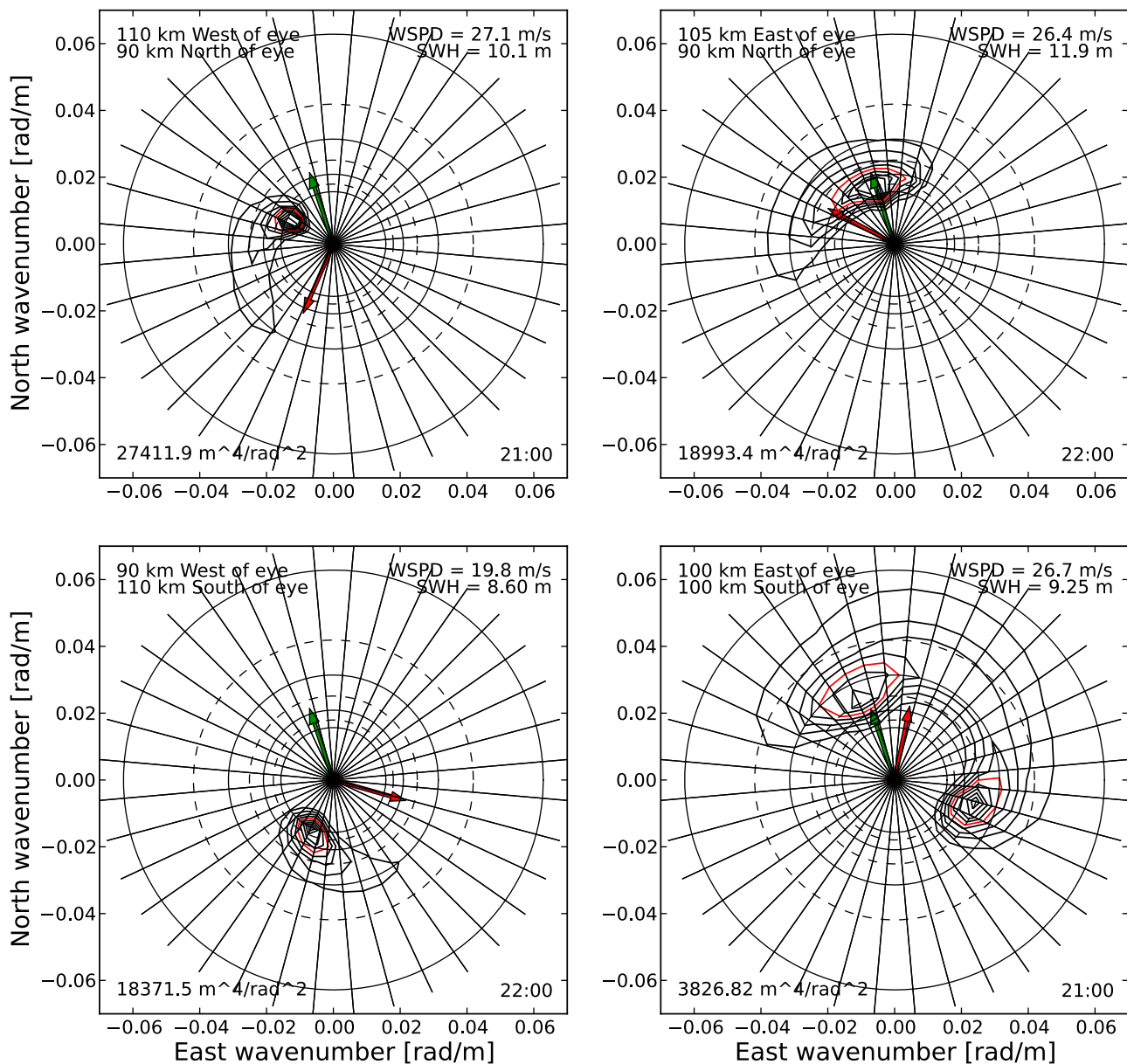


Figure 14. Modeled variance spectrum by UMWM at four locations around the storm on 24 August 1998. Location relative to storm center is indicated in the top left corner. Contours are drawn for each tenth percentile of the spectrum peak. The 50% contour is indicated in red. Spectrum peak value is given in the bottom left corner. Circles mark 100, 150, 200, 250, 300, 350, and 400 m wavelengths, from outside toward the center. Wind speed and significant wave height are shown in the top right corner. Exact time of model output is given in the bottom right corner. Red and green arrows show directions of local wind and storm translation, respectively.

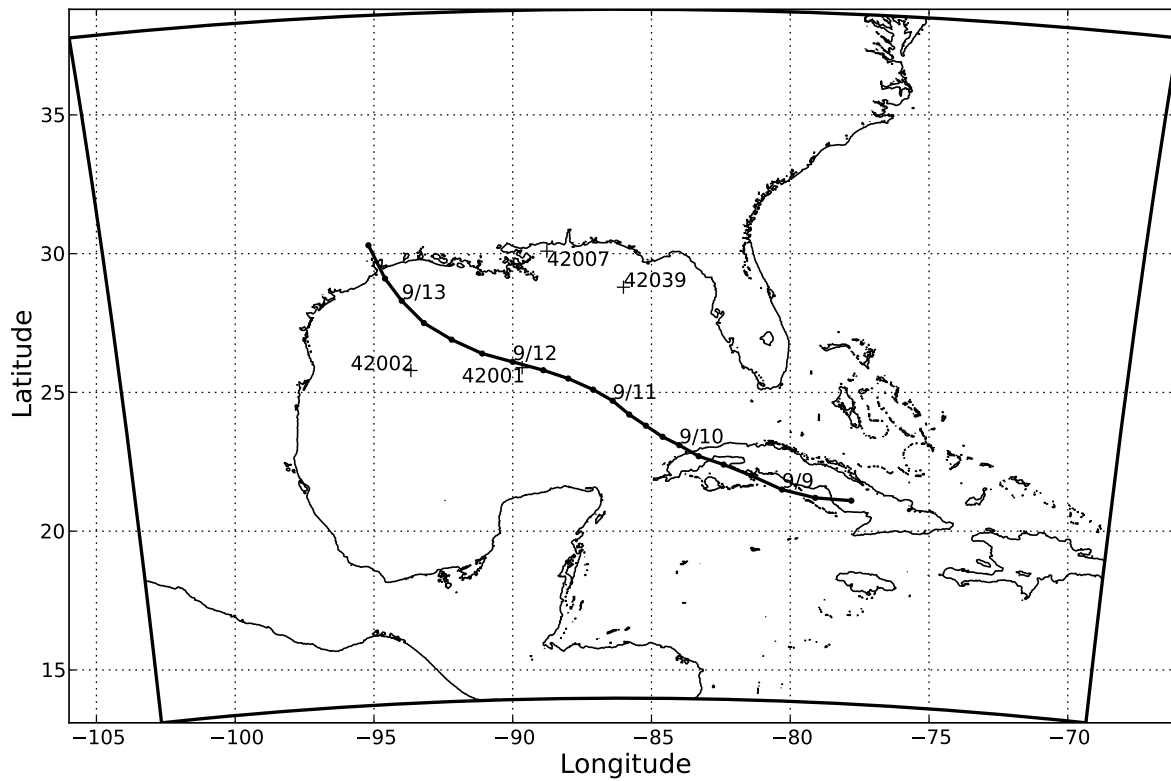


Figure 15. UMWM domain for the Hurricane Ike simulation. Best track is indicated with bold black line, and pluses indicate the locations of NDBC stations. Numbers along the track indicate the date of storm center location at each respective point.

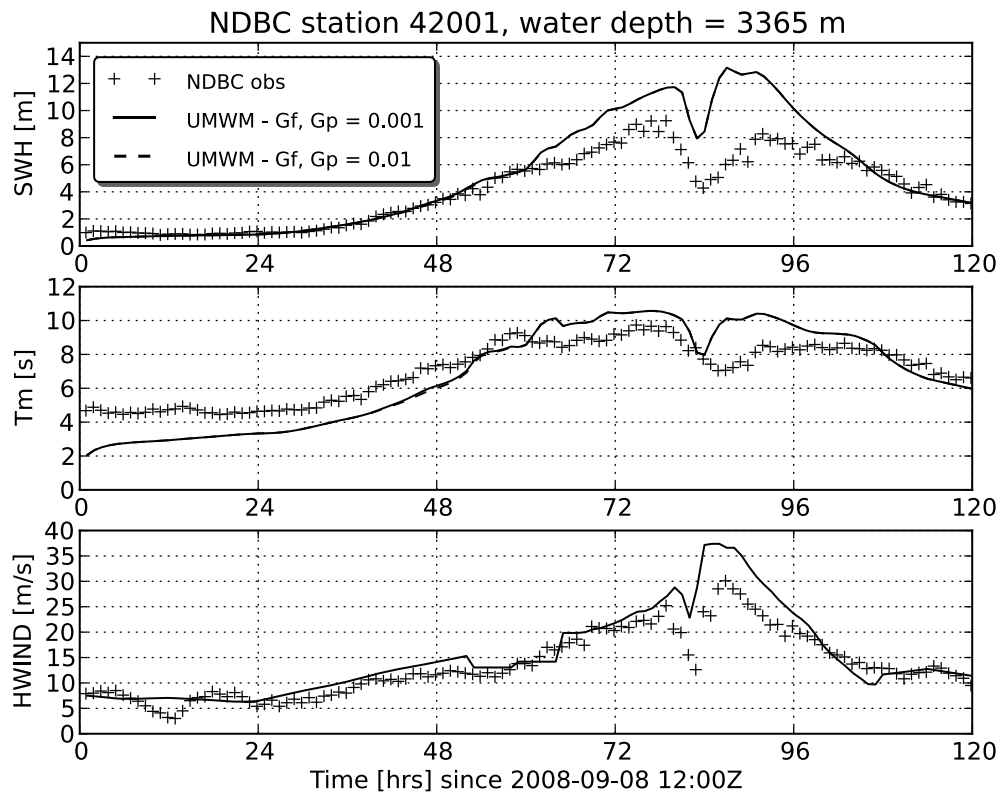


Figure 16. Comparison of significant wave height, mean period, and wind speed (HWIND) from the wave model with observations at NDBC station 42001, located near the storm track in deep water.

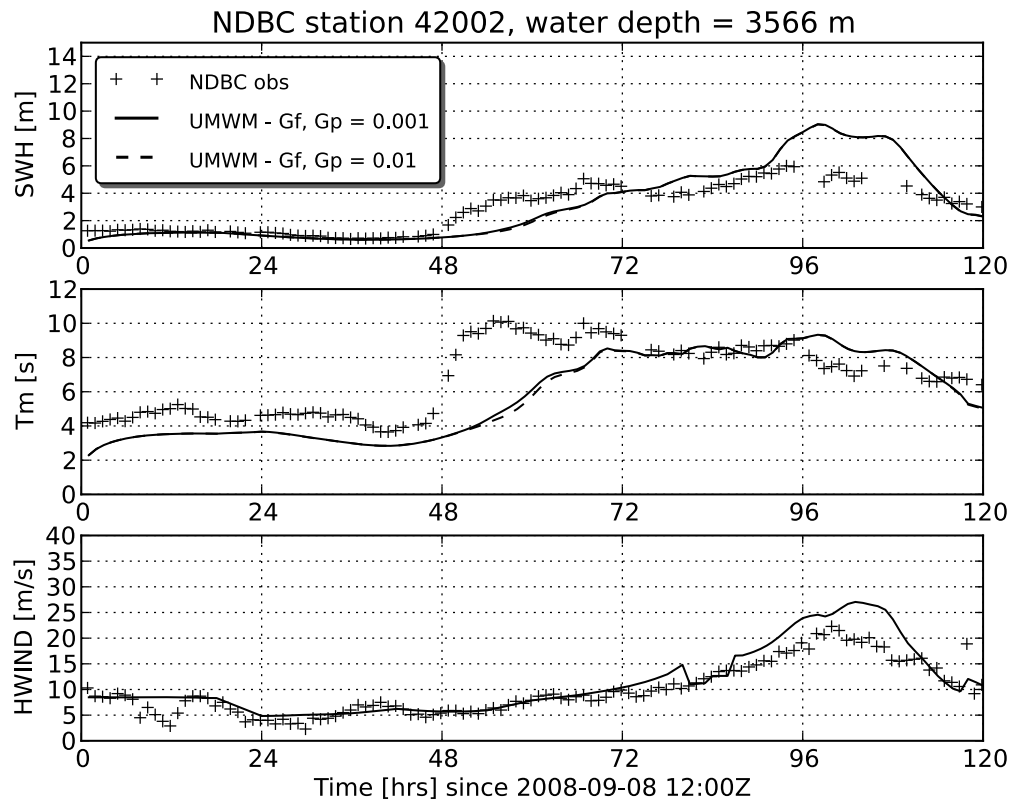


Figure 17. Same as Figure 16 but for NDBC station 42002, located on the left-hand side of the storm track.

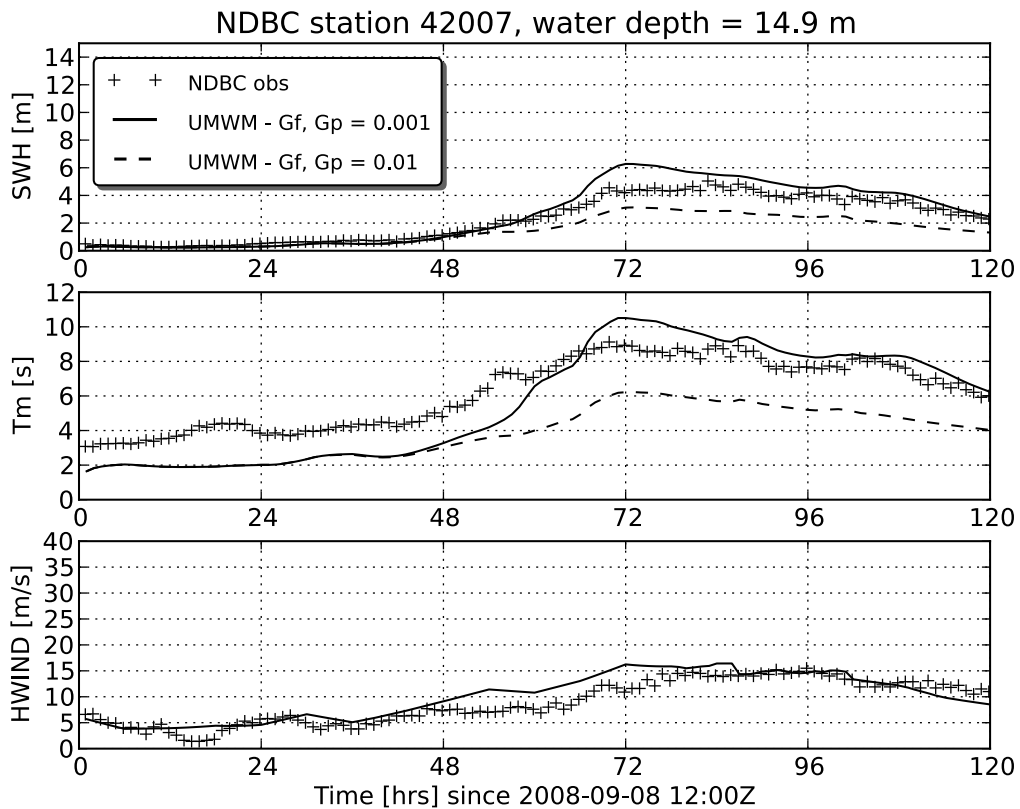


Figure 18. Same as Figure 16 but for NDBC station 42007, located on the right-hand side of the storm track in shallow water, near the coast of the United States.

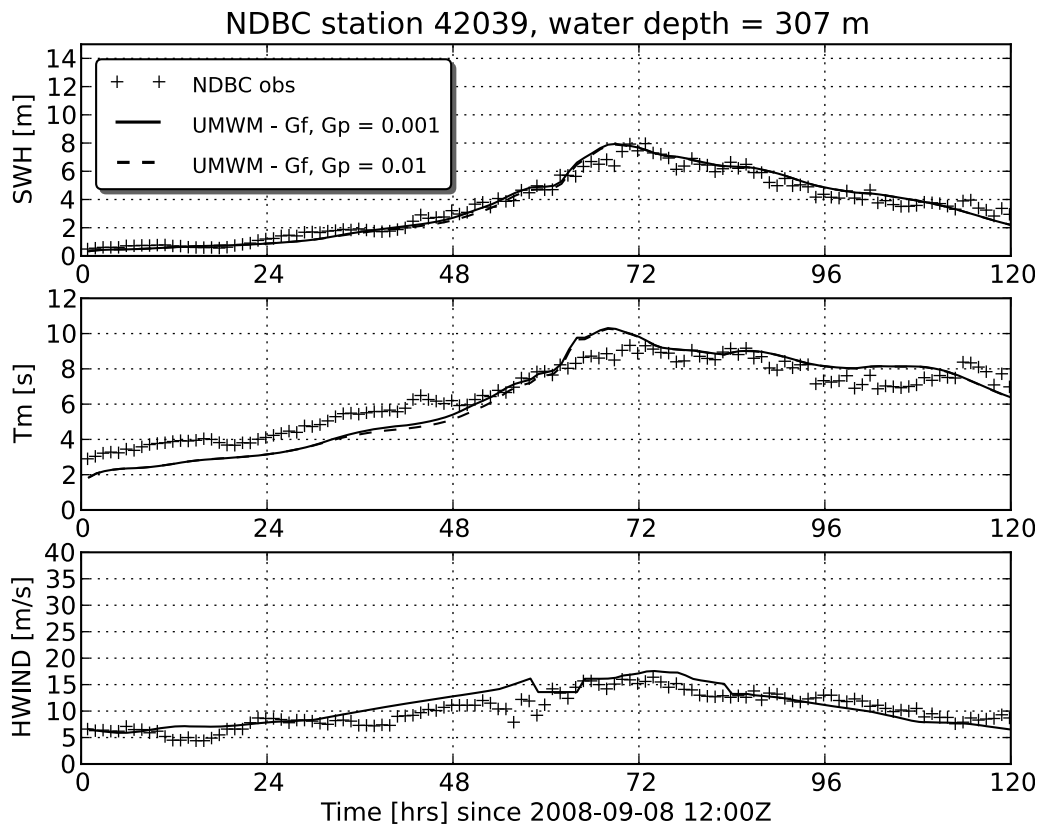


Figure 19. Same as Figure 16 but for NDBC station 42039, located on the right-hand side of the storm track.

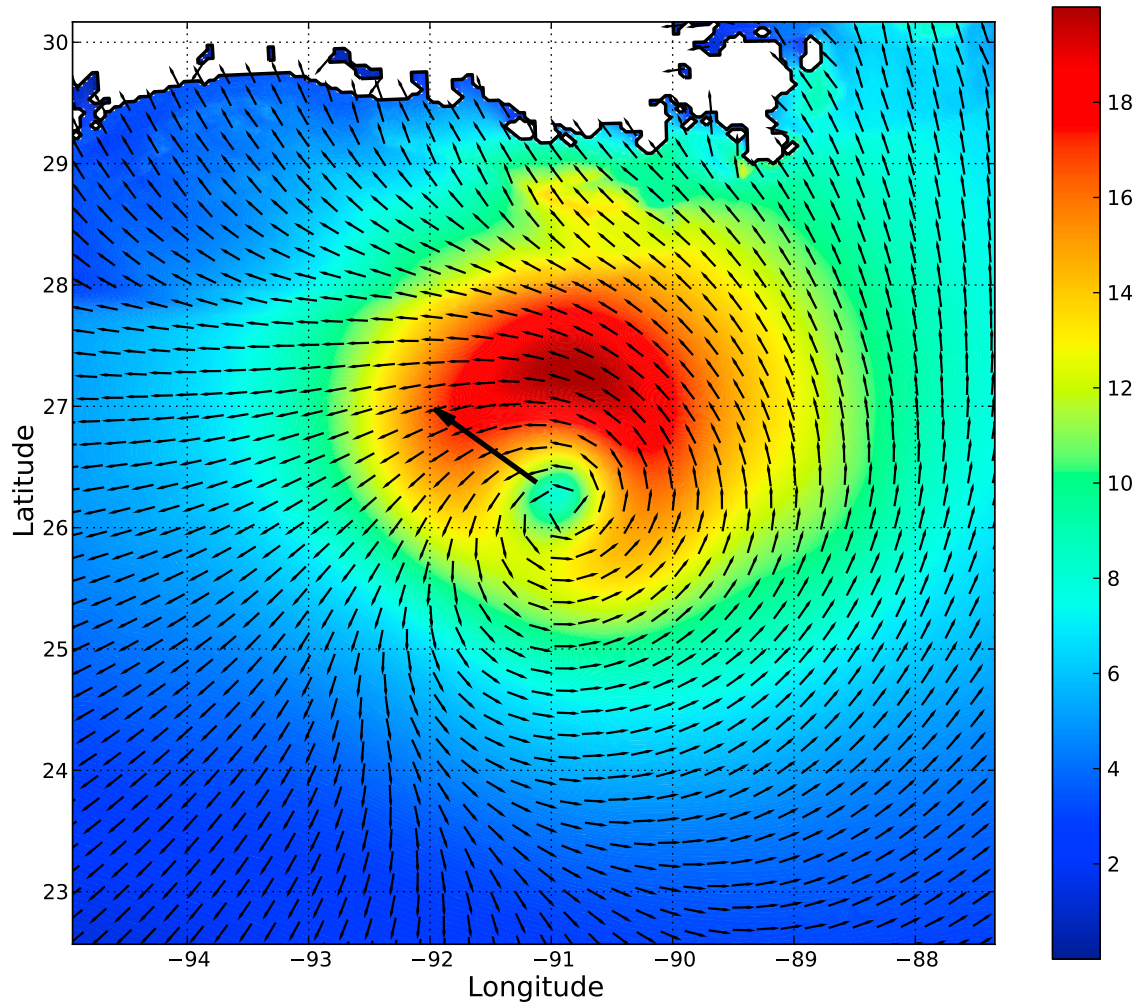


Figure 20. UMWM simulated significant wave height (color) and mean wave direction (arrows) at 06:00 UTC on 12 September 2008. Thick black arrow indicates direction of storm translation.

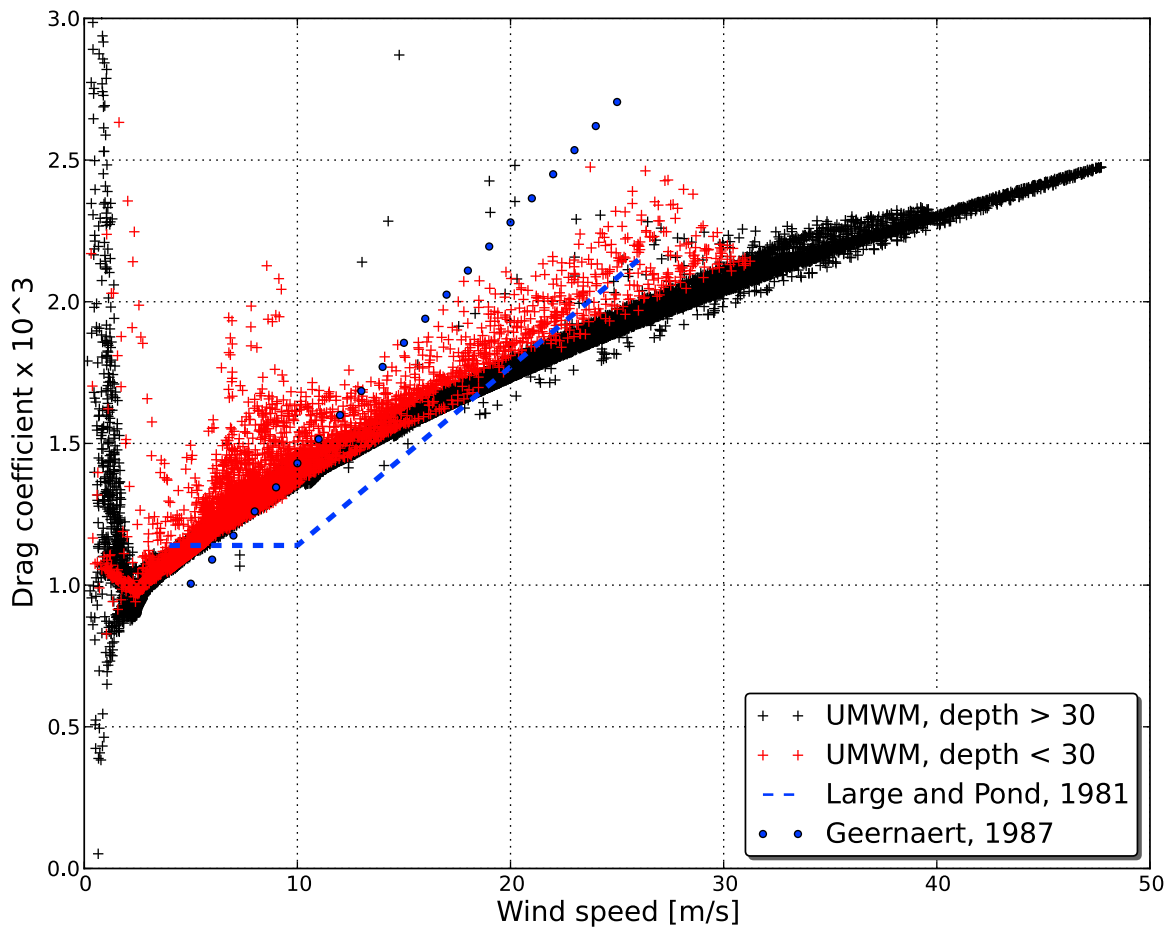


Figure 21. Drag coefficient dependence on wind speed at height of 10 m, as simulated by UMWM. Data was sampled on 06:00 UTC on 12 September 2008. Values of drag coefficient from grid cells shallower than 30 m are shown in red, and the ones from grid cells deeper than 30 m are shown in black. The dashed and dotted lines represent the observations of *Large and Pond* [1981] and *Geernaert et al.* [1987], respectively.

E^* is used to compute the advection and refraction terms described in the previous section. Finally, their contribution is evaluated by simple forward Euler differencing:

$$E^{n+1} = E_s^{n+1} - \Delta t \left[\frac{\partial[(c_g \cos\phi + u)E^*]}{\partial x} + \frac{\partial[(c_g \sin\phi + v)E^*]}{\partial y} + \frac{\partial(\dot{\phi}E^*)}{\partial \phi} \right] \quad (\text{B6})$$

The above approach is applied to the prognostic part of the spectrum. A cutoff frequency, f_c , which separates the prognostic and diagnostic parts, is proportional to the peak frequency of the fully developed Pierson-Moskowitz spectrum [Pierson and Moskowitz, 1964]:

$$f_c = 4f_{PM} = \frac{0.52g}{U_{10}} \quad (\text{B7})$$

For all bins higher than f_c , the waves are assumed to be in equilibrium with the wind (traveling in the wind direction) and their spectral densities are established from a balance of wind input and dissipation. This approach is justified by the presumption that the quasi-equilibrium range is wider in higher-wind conditions.

[100] **Acknowledgments.** We acknowledge support from NASA grant NNX07AV33G, ONR DRI ITOP grant N000140810576, ONR/NOAA NOPP TC grant N000141010162, and ONR grant N2010N567. We thank ConocoPhillips and the Norwegian Meteorological Institute for providing wave and wind measurements at Ekofisk, Magnar Reistad for preparing the wind fields from the NORA10 database, and Edward Walsh for providing the SRA spectra. We thank George Mellor for many helpful comments and suggestions. Support from the DOE National Renewable Energy Laboratory is acknowledged. The criticisms and suggestions of the reviewers have led to an improved paper.

References

- Amante, C., and B. W. Eakins (2009), ETOPO1 1 arc-minute global relief model, procedures, data sources and analysis, *NOAA Tech. Memo., NESDIS NGDC-24*, 19 pp., Natl. Geophys. Data Cent., Boulder, Colo.
- Cavaleri, L., et al. (2007), Wave modelling: The state of the art, *Prog. Oceanogr.*, *75*, 603–674.
- Chen, S. S., J. F. Price, W. Zhao, M. A. Donelan, and E. J. Walsh (2007), The CBLAST-hurricane program and the next-generation fully coupled atmosphere-wave-ocean models for hurricane research and prediction, *Bull. Am. Meteorol. Soc.*, *88*(3), 311–374.
- Donelan, M. A. (1999), Wind-induced growth and attenuation of laboratory waves, in *Wind-Over-Wave Couplings*, edited by S. G. Sajjadi, N. H. Thomas, and J. C. R. Hunt, pp. 183–194, Oxford Univ. Press, Oxford, U. K.
- Donelan, M. A. (2001), A nonlinear dissipation function due to wave breaking, paper presented at Workshop on Ocean Wave Forecasting, Eur. Cent. for Med.-Range Weather Forecasts, Reading, U. K., 2–4 July.
- Donelan, M. A., and W. J. Plant (2009), A threshold for wind-wave growth, *J. Geophys. Res.*, *114*, C07012, doi:10.1029/2008JC005238.
- Donelan, M. A., M. S. Longuet-Higgins, and J. S. Turner (1972), Periodicity in whitecaps, *Nature*, *239*(5373), 449–451.
- Donelan, M. A., J. Hamilton, and W. H. Hui (1985), Directional spectra of wind-generated waves, *Philos. Trans. R. Soc. London A*, *315*, 509–562.
- Donelan, M. A., W. M. Drennan, and A. K. Magnusson (1996), Non-stationary analysis of the directional properties of propagating waves, *J. Phys. Oceanogr.*, *26*(9), 1901–1914.
- Donelan, M. A., B. K. Haus, N. Reul, W. J. Plant, M. Stiassnie, H. C. Graber, O. B. Brown, and E. S. Saltzman (2004), On the limiting aerodynamic roughness of the ocean in very strong winds, *Geophys. Res. Lett.*, *31*, L18306, doi:10.1029/2004GL019460.
- Donelan, M. A., A. V. Babanin, I. R. Young, and M. L. Banner (2006), Wave-follower field measurements of the wind-input spectral function. Part II: Parameterization of the wind input, *J. Phys. Oceanogr.*, *36*, 1672–1689.
- Donelan, M. A., B. K. Haus, W. J. Plant, and O. Troianowski (2010), Modulation of short wind waves by long waves, *J. Geophys. Res.*, *115*, C10003, doi:10.1029/2009JC005794.
- Dudhia, J. (1993), A nonhydrostatic version of the Penn State/NCAR meso-scale model: Validation tests and simulation of an Atlantic cyclone and cold front, *Mon. Weather Rev.*, *121*, 3077–3107.
- Dysthe, K. B., K. Trulsen, H. E. Krogstad, and H. Socquet-Juglard (2003), Evolution of a narrow-band spectrum of random surface gravity waves, *J. Fluid Mech.*, *478*, 1–10, doi:10.1017/S0022112002002616.
- Fan, Y., I. Ginis, and T. Hara (2009), The effect of wind-wave-current interaction on air-sea momentum fluxes and ocean response in tropical cyclones, *J. Phys. Oceanogr.*, *39*, 1019–1034.
- Fan, Y., I. Ginis, and T. Hara (2010), Momentum flux budget across the air-sea interface under uniform and tropical cyclone winds, *J. Phys. Oceanogr.*, *40*, 2221–2242.
- Geernaert, G. L., S. E. Larsen, and F. Hansen (1987), Measurements of the wind stress, heat flux and turbulence intensity during storm conditions over the North Sea, *J. Geophys. Res.*, *92*, 13,127–13,139.
- Hasselmann, K. (1962), On the non-linear energy transfer in a gravity wave spectrum, part 1, *J. Fluid Mech.*, *12*, 481–500.
- Hasselmann, K. (1963a), On the non-linear energy transfer in a gravity wave spectrum, part 2, *J. Fluid Mech.*, *15*, 273–281.
- Hasselmann, K. (1963b), On the non-linear energy transfer in a gravity wave spectrum, part 3, *J. Fluid Mech.*, *15*, 385–398.
- Hasselmann, K., et al. (1973), Measurements of windwave growth and wind decay during the Joint North Sea Wave Project (JONSWAP), *Dtsch. Hydrogr. Z.*, *A8*, suppl., 1–95.
- Hill, C., C. DeLuca, V. Balaji, M. Suarez, and A. da Silva (2004), Architecture of the Earth System Modeling Framework, *Comput. Sci. Eng.*, *6*(1), 18–28.
- Hsiao, S. V., and O. H. Shemdin (1983), Measurements of wind velocity and pressure with a wave follower during MARSEN, *J. Geophys. Res.*, *88*, 9841–9849.
- Huang, N. E., S. R. Long, and Z. Shen (1996), The mechanism for frequency downshift in nonlinear wave evolution, *Adv. Appl. Math.*, *32*, 59–117.
- Jeffreys, H. (1924), On the formation of waves by wind, *Proc. R. Soc. A*, *107*, 189–206.
- Jeffreys, H. (1925), On the formation of waves by wind, II, *Proc. R. Soc. A*, *110*, 341–347.
- Komen, G. J., L. Cavaleri, M. Donelan, K. Hasselmann, S. Hasselmann, and P. A. E. M. Janssen (1994), *Dynamics and Modelling of Ocean Waves*, 532 pp., Cambridge Univ. Press, Cambridge, U. K.
- Large, W. G., and S. Pond (1981), Open ocean momentum flux measurements in moderate to strong winds, *J. Phys. Oceanogr.*, *11*, 324–336.
- Mellor, G. L., M. A. Donelan, and L.-Y. Oey (2008), A surface wave model for coupling with numerical ocean circulation models, *J. Atmos. Oceanic Technol.*, *25*, 1785–1807.
- Phillips, O. M. (1977), *The Dynamics of the Upper Ocean*, 336 pp., Cambridge Univ. Press, Cambridge, U. K.
- Pierson, W. J., and L. Moskowitz (1964), A proposed spectral form for fully developed wind seas based on the similarity theory of S. A. Kitaigorodskii, *J. Geophys. Res.*, *69*, 5181–5190.
- Pierson, W. J., M. A. Donelan, and W. H. Hui (1992), Linear and nonlinear propagation of water wave groups, *J. Geophys. Res.*, *97*(C4), 5607–5621.
- Powell, M. D., S. H. Houston, L. R. Amat, and N. Morisseau-Leroy (1998), The HRD real-time hurricane wind analysis system, *J. Wind Eng. Ind. Aerodyn.*, *77–78*, 53–64.
- Price, J. F., R. A. Weller, and R. Pinkel (1986), Diurnal cycling: Observations and models of the upper ocean response to diurnal heating, cooling, and wind mixing, *J. Geophys. Res.*, *91*(C7), 8411–8427.
- Reistad, M., O. Breivik, and H. Haakenstad (2007), A high-resolution hindcast study for the North Sea, the Norwegian Sea and the Barents Sea, paper presented at 10th International Workshop on Wave Hindcasting and Forecasting and Coastal Hazard Symposium, Coastal and Hydraul. Lab., Eng. Res. and Dev. Cent., U.S. Army Corps of Eng., North Shore, Hawaii.
- Reistad, M., O. Breivik, H. Haakenstad, O. J. Aarnes, and B. R. Furevik (2011), A high-resolution hindcast of wind and waves for the North Sea, the Norwegian Sea and the Barents Sea, *J. Geophys. Res.*, *116*, C05019, doi:10.1029/2010JC006402.
- Shemdin, O. H., K. Hasselmann, S. V. Hsiao, and K. Herterich (1978), Non-linear and linear bottom interaction effects in shallow water, in *Turbulent Fluxes Through the Sea Surface. Wave Dynamics and Prediction*, edited by A. Favre and K. Hasselmann, pp. 347–372, Plenum, New York.

- Tolman, H. L. (1991), A third-generation model for wind waves on slowly varying, unsteady, and inhomogeneous depths and currents, *J. Phys. Oceanogr.*, *21*, 782–797.
- Trulsen, K., and K. Dysthe (1997), Frequency downshift in three-dimensional wave trains in a deep basin, *J. Fluid Mech.*, *352*, 359–373.
- Unden, P., et al. (2002), HIRLAM-5 scientific documentation, technical report, Swed. Meteorol. and Hydrol. Inst., Norrköping, Sweden.
- Walsh, E. J., C. W. Wright, D. Vandemark, W. B. Krabill, A. W. Garcia, S. H. Houston, S. T. Murillo, M. D. Powell, F. D. Black, and F. D. Marks Jr. (2002), Hurricane directional wave spectrum spatial variation at land-fall, *J. Phys. Oceanogr.*, *32*, 1667–1684.
- Wright, C. W., E. J. Walsh, D. Vandemark, and W. B. Krabill (2001), Hurricane directional wave spectrum spatial variation in the open ocean, *J. Phys. Oceanogr.*, *31*, 2472–2488.